Nano Scale Disruptive Silicon-Plasmonic Platform for Chip-to-Chip Interconnection

Report on optical properties of quantum dot layers and polymer nanocomposites

Deliverable no.:	D 4.2
Due date:	04/31/2013
Actual Submission date:	04/31/2013
Authors:	UVEG, UGENT, AIT
Work package(s):	WP4
Distribution level:	RE[1] (NAVOLCHI Consortium)
Nature:	document, available online in the restricted area of the NAVOLCHI webpage

List of Partners concerned

Partner number	Partner name	Partner short name	Country	Date enter project	Date exit project
4	RESEARCH AND EDUCATION LABORATORY IN INFORMATION TECHNOLOGIES	AIT	Greece	M1	M36
5	UNIVERSITAT DE VALENCIA	UVEG	Spain	M1	M36
7	UNIVERSITEIT GENT	UGent	Belgium	M1	M36

---

[1]   **PU** = Public
        PP = Restricted to other programme participants (including the Commission Services)
        RE = Restricted to a group specified by the consortium (including the Commission Services)
        CO = Confidential, only for members of the consortium (including the Commission Services)

Deliverable Responsible

Organization: Athens Information Technology
Contact Person: Emmanouil-Panagiotis Fitrakis
Address: 19.5 Km Markopoulo Ave.
19002 Peania, Attiki, Greece
Phone: +30 210 668 2721
Fax:
E-mail: mfitrakis@ait.gr

Executive Summary

In this deliverable we include research devoted on optical properties of quantum dot (QD) layers and polymer nanocomposites, that is, all materials involved in the fabrication of the plasmonic amplifier and photodetector. QDs can be deposited by solution processing techniques to form close-packed layers on top of different substrates (glass, glass/ITO, Si/SiO$_2$, …) or dispersed in dielectric polymers (QD nanocomposites) to constitute the gain material for plasmonic amplifiers. Other interesting nanocomposites for plasmonic devices are based on metal nanoparticles dispersed/synthesized in polymers (dielectric and conductive) that can be used to form complex metal nanostructures (plasmonic waveguides, couplers, …), nano/microelectrodes, plasmonic photoconductors, etc.

Change Records

| Version	Date	Changes	Author
1	2013-04-12	Nanocomposites	Isaac Suárez
2	2013-04-23	QDs, LbL and Polymers	P. J. Rodríguez-Cantó
3-5	2013-05-10	Edition UVEG part	J. P. Martínez Pastor
6	2013-05-20	Addition UGent part	Z. Hens
7	2013-05-23	Edition AIT	Emmanouil-P. Fitrakis Ioannis Tomkos
8	2013-05-25	Edition UVEG	J. P. Martínez Pastor

INDEX

FP7-ICT-2011-7
Project-No. **288869**
NAVOLCHI – D4.2

Deliverable Report
Last update 01/31/2012
Version 1

1. Introduction and objectives

A signal generated at the plasmonic transmitter chip (laser plus modulator) has to be measured by a plasmonic receiver in order to be processed electronically. For this purpose, the receiver needs to accomplish the following conditions. Firstly, low-level signals coupled to a plasmonic waveguide (photons are transformed into propagating Surface Plasmon Polaritons - SPPs-) will be amplified before the input of the detector in order to enhance the sensitivity of the receiver. Secondly, the incoming signal in the detector will convert the amplified SPPs into an electrical signal. With the intention to improve the chip-to-chip interconnection integration, amplifier and detector will be designed into the same silicon substrate [1], as it is illustrated in Fig. 1.1. The plasmonic amplifier (on the left of Fig. 1.1) consists of a gold (Au) nanostripe surrounded by a polymer with active centers inside (SU-8 + Quantum Dots). The polymer acts as a dielectric with gain that can compensate for the losses of the gold waveguide when the active centres were optically or electrically pumped.
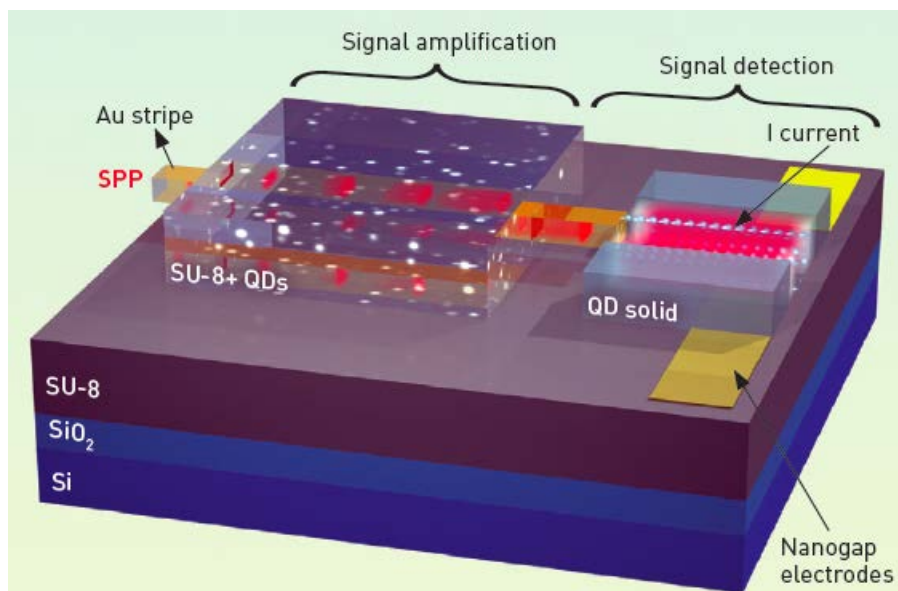
Figure 1.1: Plasmonic receiver with SPP amplifier and a photodetector *(from Ref. 1)*.

The photodetector (on the right of Fig. 1.1) will consist of a conductive layer of PbS (or PbSe) quantum dots (QDs), whose thickness will be optimized to assure the maximum responsivity of the device, able to generate an electrical current as a response of the incoming photons [2]. Reported photoconductive responsivities in recent literature are in the range of 0.1-3.9 A/W for a PbS QD monolayer in a nanogap-electrode structure [3], larger than 100 A/W in the case of microgap-electrode structures with PbS layers thicker than 200 nm [4] and more than 10^6 A/W in a MOS microgap-structure based on a PbS layer (60-80 nm thick) on graphene [5]. The QD-solid (conductive layer of QDs) approximation is considered one of the latest advanced concepts for photodetection, given the high absorption of quantum dots, the low cost of the solution processing technique used to deposit the material as well as its integration in Si technology. Furthermore, this concept can be easily combined with plasmonic layers based on metal nanoparticles, because an enhancement of the responsivity is expected due to light trapping effect at the band edge of the QD-solid [4].

FP7-ICT-2011-7   **Deliverable Report**
Project-No. **288869**   Last update 01/31/2012
NAVOLCHI – D4.2   Version 1

To achieve the goals proposed in Navolchi, we have addressed:

1) For Plasmonic Amplifiers

- Synthesis and characterization of infrared colloidal nanostructures based on PbS, PbSe or Mercury based materials.
- Preparation and characterization of close packed mono- and multilayers of these quantum dots.
- Preparation and characterization of polymer based nanocomposites by dispersing such nanoestructures: micro-patterning.
- Optical Characterization of those nanocomposite thin films for waveguiding and amplification purposes.
- QD-based structures for Electrical injection.
- Special plasmonic nanocomposites for the fabrication of metal nanostructures.

2) For Photodetectors:

- Synthesis and characterization of infrared colloidal QDs (PbS and PbSe).
- Preparation and characterization of QD-solids based on these nanoestructures.
- Electrical Characterization of the fabricated devices. *The results of this characterization will be included in Milestone 20*.

The different sections of this deliverable will include a summary of results on these different topics. The beginning of our research to define waveguides with QDs was dated 7-8 months before the official date of Navolchi start (1st November). Several reasons moved us to begin with QDs emitting at the visible: i) the literature background on CdSe, CdSe and CdTe QDs was more important than for QDs emitting at the infrared, ii) the quantum yield of core-QDs based on these materials was larger than in the case of QDs emitting at the infrared, and iii) at this time most of our optical equipment to characterize materials and waveguides was at visible wavelengths. In fact, the first paper by the UVEG team using these QDs was published in October 2011 [6]. In this deliverable we devote some sections to such preliminary work. Furthermore, electrical injection devices based on colloidal QDs are also an objective of the project (not in the first half period), and preliminary evaluations have been made (by UGENT, IMCV and UVEG teams) for visible wavelengths too, mostly by reasons i-ii. Of course, since the first months of Navolchi launching date, once efficient colloidal nanostructures emitting at the infrared were available at appropriate quantities, research moved to the study of the same polymers doped with these nanostructures, mainly based on PbS and PbS as their core material.

2. Synthesis and optical properties of colloidal QDs and nanostructures

2.1. QDs emitting at visible wavelengths

As explained in the introduction, QDs emitting at visible wavelengths have been or are being used for preliminary or exploratory investigations, given the vast literature background on these materials. The chemistry to prepare nanocomposites or QD-solid layers has been found to be independent of the QD material and hence the implementation of infared emitting nanoscomposites for waveguiding/amplification and structures for electrical injection purposes is straightforward.

The materials (CdS, CdTe and CdSe core-QDs; core-shell CdSe/ZnS QDs) are synthesized by standard methods by the spin-off company of the UVEG group and dispersed in appropriate concentrations on different polymers. These colloidal solutions will be transformed in nanocomposite thin films once deposited on Si-SiO$_2$ substrates.
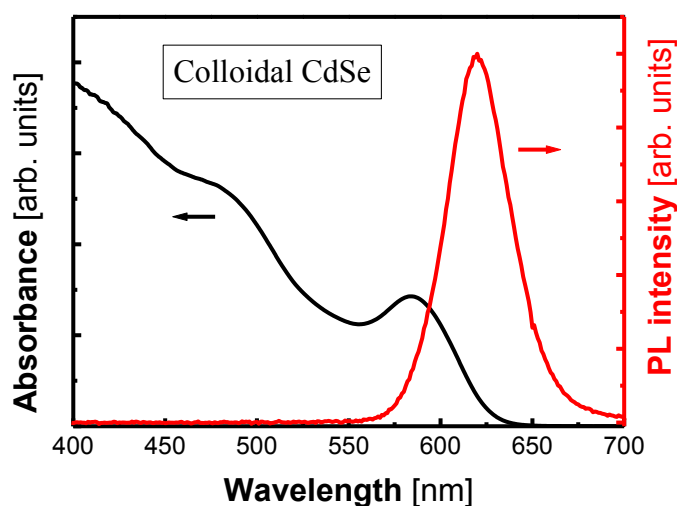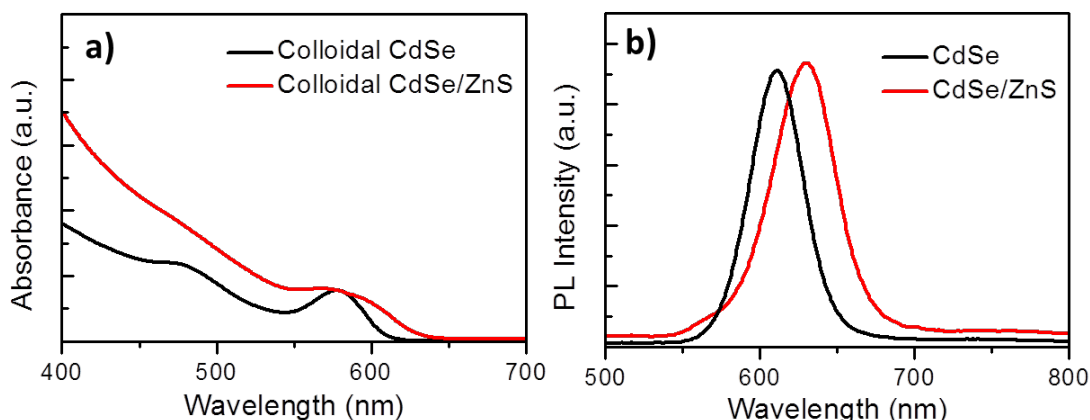

Figure 2.1: Absorbance (black line) and PL (red line) spectra of CdSe QDs.

Figure 2.1 shows the absorption and photoluminiscence (PL) spectra of CdSe QDs, as the most common material used in this work for: preparation of polymer nanocomposites, thin film deposition with controlled thickness (spin-coating) and patterning (linear waveguides, for example), as the main ingredients for the construction of the plasmonic amplifiers by using optical pumping. The PL line is centred at 620 nm and has a Full Width at Half Maximum (FWHM) of 40 nm. The absorbance peak corresponding to the ground state exciton transition is measured at 580 nm, whereas an excited state transition is observed at around 480 nm. Absorption increases continuously for short wavelengths and it is virtually zero for wavelengths longer than 650 nm.

An important strategy to improve the surface passivation of core QDs is their overgrowth with a shell of a second semiconductor, resulting in core-shell nanostructures. The synthesis of CdSe/ZnS QDs is made by the so-called SILAR (successive ion layer adsorption and reaction) method [7]. The ZnS shell passivizes the surface of the CdSe core, but also acting as a potential

barrier for carrier confinement. As a result, fluorescence efficiency and stability against photooxidation are significantly improved and the sensitivity of the optical properties to changes in the local environment of the QDs' surface, induced by the presence of oxygen or water molecules, is reduced. At the same time, the shell reduces the number of surface dangling bonds, which can act as trap states for charge carriers, and thereby increasing the emission quantum yield. Figure 2.2 shows the absorption (a) and PL (b) spectra for both CdSe core and CdSe/ZnS core-shell QDs. The presence of the ZnS shell growth is accompanied by a small red shift (10–15 nm) of the excitonic peak in absorption and PL spectra, which is attributed to a weaker potential well (some hundreds of meV) as compared to organic ligands (several eV [8]**¡Error! Marcador no definido.**]).
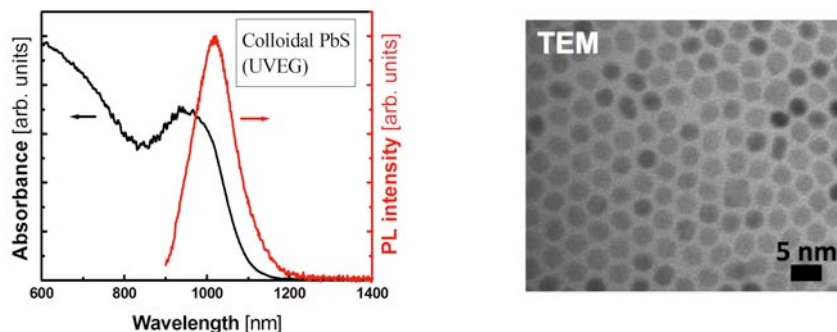

Figure 2.2: Absorbance (a) and PL (b) spectra of CdSe core (black lines) and CdSe/ZnS core-shell (red lines) QDs in octane.

2.2. QDs and nanostructures emitting at infrared wavelengths

a. PbS QDs (UVEG)

The synthesis of QDs for IR is based on the hot injection of metal-organic precursors into coordinating/non-coordinating solvents at elevated temperatures. This strategy is established to be the mainstream strategy in the synthesis of high quality semiconductor nanocrystals. The synthesis of PbS (and PbSe) QDs is again developed by the spin-off company of the UVEG group. Typically, lead oleate and bis(trimethylsilyl) sulfide (TMS) are used as precursors and fixing a Pb to S precursor ratio to 2:1, which is within the typical range employed in cadmium chalcogenide and lead chalcogenide nanocrystal synthesis [9]. A slow cooling following sulfur precursor injection is employed to obtain narrow size distribution and well-defined excitonic features in absorption and emission spectra, as observed in Fig. 2.3.

FP7-ICT-2011-7   **Deliverable Report**
Project-No. **288869**   Last update 01/31/2012
NAVOLCHI – D4.2   Version 1

Figure 2.3: Absorption and PL spectra of as-synthesized PbS colloidal QDs in toluene (left) and TEM image of these PbS QDs.

Figure 2.3 shows the absorbance spectrum of acid oleic-capped PbS colloidal QDs in toluene. As can be observed PbS QDs showed a well-defined excitonic peak centred at around 870 nm. The average size of them was 3.2 nm (Fig. 2.3, right), approximately, as calculated from the equation proposed by Moreels *et al.* [10]:

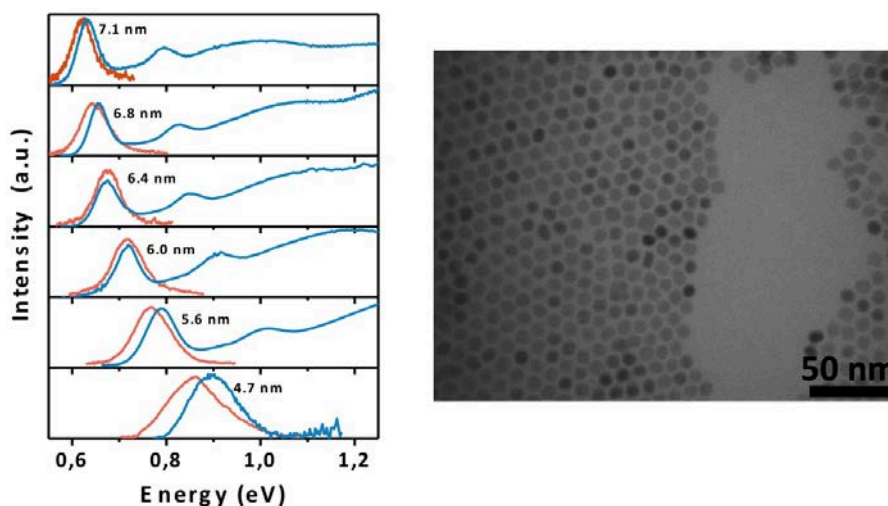$$E^0 = 0.41 + (0.0252d^2 + 0.283d)^{-1} \qquad\qquad (2.1)$$

where E_0 is the effective bandgap (1.30 eV in the case of QDs in Fig. 2.3) and d is the PbS QD diameter in nm.

These PbS QDs are mainly used for developing QD-solid films by the layer-by-layer method, as described below, as the basis for photodetectors. For this reason the QDs are produced for having and absorption bandedge around 1000-1100 nm (Fig. 1) in order to compare with most of results published in literature (Refs. 2-5, as some of the most representative). Once optimized the main parameters of the devices the layers will be formed by using PbS (or PbSe) with bandedge beyond 1500 nm. The colloidal QDs are purified by selective precipitation using non-solvents (acetone/methanol mixture). A ligand exchange reaction is carried out by dispersing oleate-capped PbS in oleylamine, which has the same molecular size as oleic acid but exhibits less affinity to PbS. In this way, the bond between PbS and oleylamine becomes weaker than oleate, as required for the subsequente formation of the QD solid, as described below. After this partial ligand exchange, absorption is blue-shifted by 10 nm. QDs are purified again by selective precipitation with methanol and then redispersed in octane at a concentration of 20 mg/mL, typically.

b. PbSe QDs (UVEG)

The synthesis of monodisperse PbSe QDs with different sizes is very similar to that described above for PbS QDs, on the basis of Ref. 11. Figure 2.4 shows the absorption and emission spectra for different size PbSe QDs: the ground state exciton transition is tuned in the range 1300-1900 nm. Some basic work on these QDs was recently published regarding the effect of quantum size confinement on their optical properties as a function of temperature and hydrostatic pressure [8]; this effect comes from the small effective mass and its particular variation with temperature and pressure in this material.

FP7-ICT-2011-7

Project-No. **288869**

NAVOLCHI – D4.2

Deliverable Report

Last update 01/31/2012

Version 1

Figure 2.4: Absorption and PL spectra of colloidal PbSe QDs with different sizes ranging from 4.7 to 7.1 nm (left); TEM image of PbSe QDs with an average size of about 7 nm (right).

c. PbS QDs (UGENT)

PbS quantum dots were synthesized using procedures established before at UGent [12] and have been supplied to UVEG for further characterization. Figure 2.5 shows the PL spectra of the PbS QDs used initially in this project to check the plasmonic coupling in the IR. The PL line is centred at 1550 nm and has a FWHM of 200 nm.
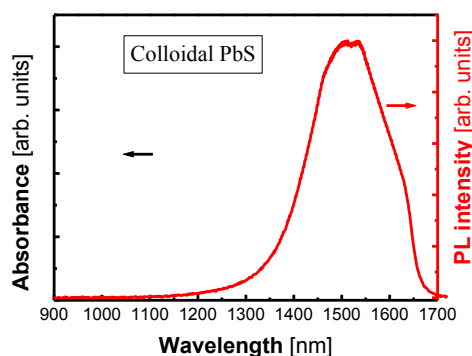
Figure 2.5: Absorbance (black line) and PL (red line) spectra of PbS QDs**.**

d. PbS/CdS QRs (UGENT)

PbS/CdS multiple dot-in-rod structures were synthesized using procedures established before at UGent [13] (see also MS17 report) and have been supplied to UVEG for further characterization. Figure 2.6 shows the absorption and PL spectra of PbS/CdS semiconductor nanorods to be tested for amplification purposes. The PL line is centred at around 1350 nm and has a FWHM of 280 nm. Absorption is very low at the ground state exciton transition at the core material, but increases abruptly at the bandedge corresponding to the shell material. Then, the effective Stokes shift is larger than 700 nm.
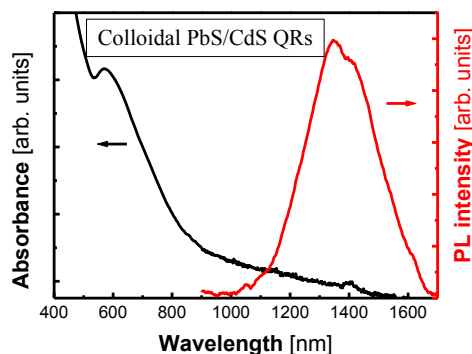
Figure 2.6: Absorbance (black line) and PL (red line) spectra of PbS/CdS semiconductor nanorods.

e. *Partially exchanged PbS/CdS QRs (UGENT)*

Partially exchanged PbS/CdS dot-in-rod structures were synthesized using procedures established before at UGent (see MS17 report). Figure 2.7 shows a PL spectrum of PbS/CdS partially exchanged (PER) nanostructures to be tested for amplification purposes. The PL line shows two peaks centred at 1050 and 1150 nm, and the FWHM extends to around 300 nm. The absorption (data not shown) increases continuously for short wavelengths and shows a peak at around 450 nm corresponding to the ground state exciton of the CdS shell. For longer wavelengths absorption decreases and it is negligible for wavelengths longer than 1000 nm. Again, the Stokes shift is 600-700 nm.
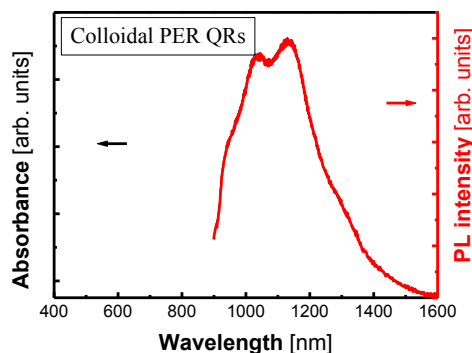

Figure 2.7: Absorbance (black line) and PL (red line) spectra of PbS/CdS partially exchanged nanorods.

f. *PbSe/CdSe QRs (UGENT)*

PbSe/CdSe dot-in-rod structures were synthesized using procedures established before at UGent [13] (see also MS17 report). Figure 2.8 shows the PL spectrum of PbSe/CdSe semiconductor nanorods to be tested for amplification purposes. The PL is centred at 1400 nm and the FWHM is around 300 nm. The absorption spectrum (data not shown) increases monotonically from long to short wavelengths and hence there are not a well defined Stokes shift.
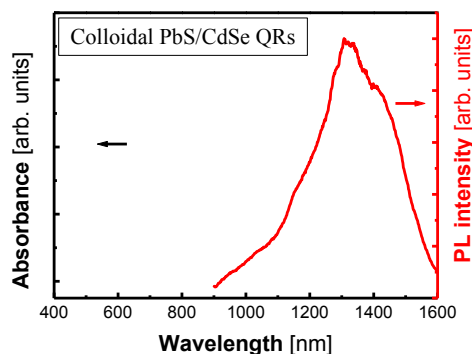
FP7-ICT-2011-7
Project-No. **288869**
NAVOLCHI – D4.2

Deliverable Report
Last update 01/31/2012
Version 1

Figure 2.8: Absorbance (black line) and PL (red line) spectra of PbS/CdSe QRs made in UGENT.

2.3. Amplified spontaneous emission of Pb chalcogenide based quantum dots by transient absorption spectroscopy

Different types of Pb-chalcogenide nanostructures were investigated as potential gain materials for on-chip amplification in the near-infrared, especially for applications at 1550 nm. Two major hurdlestones towards optical amplification using Pb-based colloidal nanocrystals are [14]:

-   High degeneracy of the band edge requiring multi-excitons for population inversion.
-   Fast non-radiative multi-exciton recombination through Auger ionization.

Different approaches have been suggested in literature, either reducing the Auger rate [15] or lifting the effective degeneracy of the band-edge [16]. Both approaches were succesfully applied to Cd-based nanocrystals emitting in the visible part of the spectrum (<700 nm). Extending these approaches tot he near-infrared is not trivial since the techniques used for the visible nanocrystals are not readily available fort he near-infrared emitting Pb-compounds. PbX nanocrystals show multi-exciton lifetimes in the order of 50 picoseconds, requiring up to 4 excitons per nanocrystal. In practice, this would require very high threshold current densities in the order of kA/cm^2 to reach optical transparency and further amplification.
One approach to reduce the Auger rate and lift the degeneracy is to use 1D nanostructures. Indeed, it is by now well known that the Auger rate scales with the nanocrystal volume. We propose to use rod-like, so-called 1-dimensional, nanostructures for this purpose. In particular we use PbS nanorods synthesized according to Justo et al. [13]. Intervalley coupling already lifts part of the degeneracy of the emitting state in PbSe nanocrystals due to fine structure splitting [17] and it is assumed that 1D structures would further enhance this fine-structure splitting.
We investigated spherical nanocrystals of PbS, nanorods of PbS with dimensions of 4 nm x 12 nm (denoted ‚short') and 3.7 nm x 28 nm (denoted ‚long') (diameter x length) using a white light transient absorption setup at the TU Delft. Here, samples are excited using 700 nm, 200 fs pulses and the change in absorbance is probed using broadband light generated in a sapphire crystal. The quantity $\Delta\alpha = \alpha - \alpha_0$, i.e. the difference in absorption with and without pump is measured as a function of time and wavelength. A negative value for this quantitiy implies decreased absorbance, also termed ‚bleach'. Optical transparency, a prerequisite for optical amplification, would imply:

FP7-ICT-2011-7
Project-No. **288869**
NAVOLCHI – D4.2

Deliverable Report
Last update 01/31/2012
Version 1

$$\frac{\Delta\alpha}{\alpha_0} = -1 \qquad\qquad\qquad (2.2)$$

Only the short rods show optical gain, i.e. a normalized bleach below -1. A typical (normalized) bleach spectrum is shown in figure 2.9. However, we only cross the transparency threshold under extremely high fluence laser excitation. Moreover, the transparency only lives for ca. 10 ps (see figure 2.10). The normalized bleach spectrum indicates that optical gain develops on the low energy side (longer wavelengths) of the steady state emission spectrum. This correlates to the fine structure splitting suggested by De Geyter *et al.* [17] where carriers would indeed cool to the lowest energy states, yielding the bleach at the low energy side of the spectrum. We do not observe a decrease in gain threshold value, nor a significant shortening of the Auger lifetime. A possible explanation for this is to be found in the morphology of the nanorods. As demonstrated previously, the rods are not single crystalline but are built from smaller segments, strongly resembling an attachment of smaller spherical crystals into a rod-like object. We believe the structural inhomogeneity within a single rod breaks the 1D character, thus removing any possible new features that could arise from the 1D confinement in a larger volume.
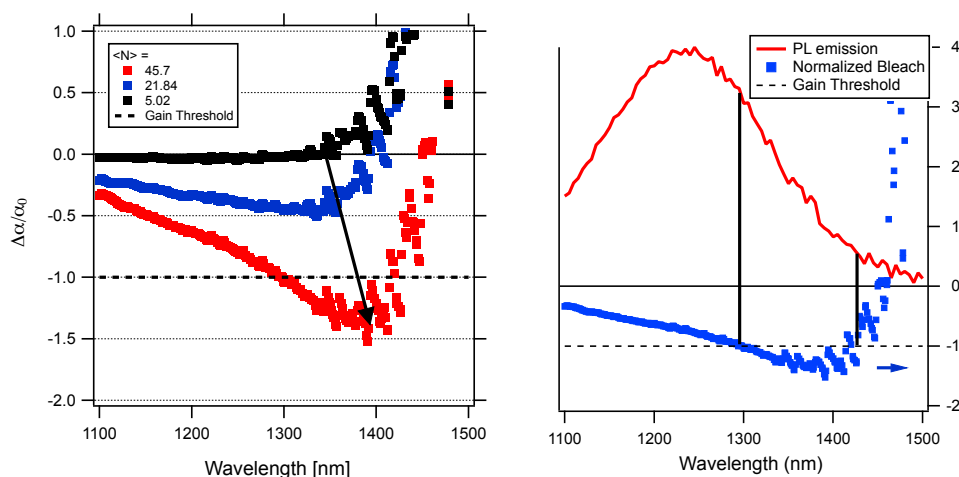
Figure 2.9: (left) Normalized bleach spectrum for short PbS nanorods under different excitation fluences, expressed in absorbed pump photons per nanorod <N>. The spectra are obtained 2.5 picoseconds after photo-excitation at 700 nm. (right) Normalized bleach spectrum with gain band extrapolated to steady state photoluminescence spectrum.
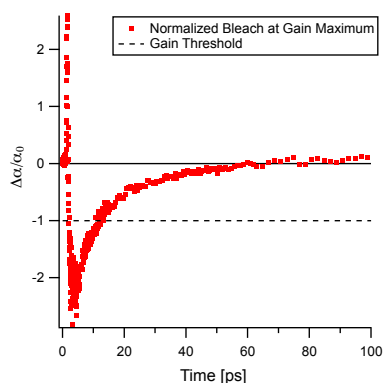

Figure 2.10: Normalized bleach as a function of time (or equivalent probe delay) for a fluence of 56 absorbed photons per nanorod.

FP7-ICT-2011-7   **Deliverable Report**
Project-No. **288869**   Last update 01/31/2012
NAVOLCHI – D4.2   Version 1

Future materials under investigation are HgX compounds and InX/CdS heterostructures. For example, HgTe can be tuned to emit in the near-infrared with high quantum yield and short radiative lifetimes. Since Hg-salts are direct semiconductors with a band gap in the gamma-point of the Brillouin zone, only a doubly degenerate band edge is to be expected. This would imply population inversion could occur at 1 exciton per nanocrystal. The Auger lifetime is to be investigated but considerations from bulk (different electron and hole masses, large confinement energy) could imply lower Auger rates than the Pb-salts. As was recently shown [18], InP/CdS displays a type II band-offset, potentially allowing for single-exciton gain in the near-infrared.

3. Optical properties of colloidal quantum dot monolayers

3.1. Absorption enhancement in quantum dot monolayers

We have analyzed the absorption cross section σ_f of PbS and CdSe quantum dots (QDs) in close-packed, one component monolayers. These materials have been chosen since CdSe is the most widely used colloidal QD and, as such, a reference material, while PbS QDs can be tuned to have its band gap at telecom wavelengths. As compared to literature data on the absorption cross section in diluted dispersions ($\sigma_{0,s}$) of both materials [19,10], we find that σ_f can be enhanced up to a factor of 4 (CdSe) or 5 (PbS). For example, in the case of PbS QDs, the enhancement $E = \sigma_f/\sigma_{0,s}$ shows a marked, resonance-like diameter dependence, with a maximum value for QDs of around 4 nm. Similar results are obtained for CdSe. We also show a strong dependence on the superlattice parameters by studying the effect of the interparticle spacing on fixed size CdSe nanocrystals. Moreover, E is largely wavelength independent, which was validated for PbS. We show that the value and the layer parameter-dependence of E for both PbS and CdSe can be quantitatively described by considering the dipolar coupling between neighboring QDs in the close packed film. According to this description, the resonance behavior results from the condition for optimal coupling, where the mutual enhancement of the electric fields of neighboring QDs is maximized. In this way, we demonstrate that light absorption by a close packed film of quantum dots is a joint property of the individual QDs and the QD superlattice, thereby showing for the first time a truly collective optical effect in colloidal nanocrystal superlattices.
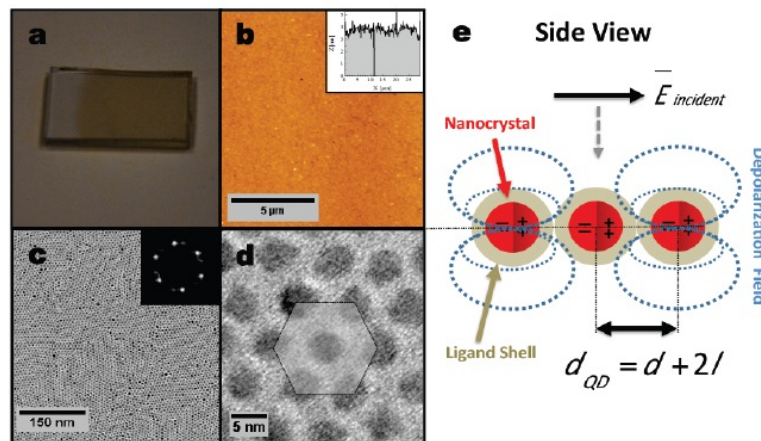

Figure 3.1: Langmuir-Blodgett monolayer of PbS quantum dots. (a) Contrast picture of a monolayer of PbS quantum dots ($d = 5$nm) on a glass surface (2cm×1cm) showing homogeneous cm2 coverage. (b) Atomic force microscope scan of the same PbS monolayer indicating excellent area uniformity (inset: cross section). (c) Larger area TEM image showing the PbS quantum dot superlattice with local hexagonal ordering (inset: Fourier transform image). (d) zoomed-in TEM image showing the individual quantum dots and their interdistance. (e) Side view schematic of monolayer subject to incident field polarized in-plane. The relevant geometrical parameters are indicated by d_{QD}, d and l, respectively the (nearest-neighbor) interdot-distance, QD size and ligand length.

For this study, we make use of monodisperse batches of CdSe and PbS QDs stabilized by carboxylate ligands. They have been synthesized following literature recipes [19,10], with diameters d_{QD} ranging from 2.5 to 6.2 nm for CdSe and 2.5 to 8 nm for PbS. In both cases, QD monolayers are formed by spreading a QD dispersion on a Langmuir trough [20], followed by the transfer of the Langmuir film to a glass substrate using Langmuir-Blodgett deposition. As

FP7-ICT-2011-7   **Deliverable Report**
Project-No. **288869**   Last update 01/31/2012
NAVOLCHI – D4.2   Version 1

shown in Figure 3, this results in homogeneous monolayers over cm² areas, with typical surface coverages as determined by atomic force microscopy (AFM) of 95% or more. In addition, transmission electron microscopy (TEM) demonstrates that the monolayers have a locally hexagonal ordering. The QD surface density (Ns) is determined from TEM micrographs (Figure 3(c)), while the QD interdistance – written as $d_{QD} + 2l$ where l denotes the thickness of the ligand shell – is obtained from more detailed TEM analysis (see Figure 3(d)). The absorption cross section σ_f of a QD in these close packed monolayers is calculated from the absorbance A and the reflectance R:

$$\sigma_f = \ln 10 \times \frac{A - R}{N_s} \tag{3.1}$$

In this expression, scattering is neglected since the wavelengths used (> 335 nm) are much larger than the quantum dot diameter. The correction of the absorbance for reflection is typically very small (<10%). To calculate the absorption enhancement, we combine the experimental values of σ_f with published values for $\sigma_{0,s}$, where we work at 400 nm for PbS and at 335 nm for CdSe.
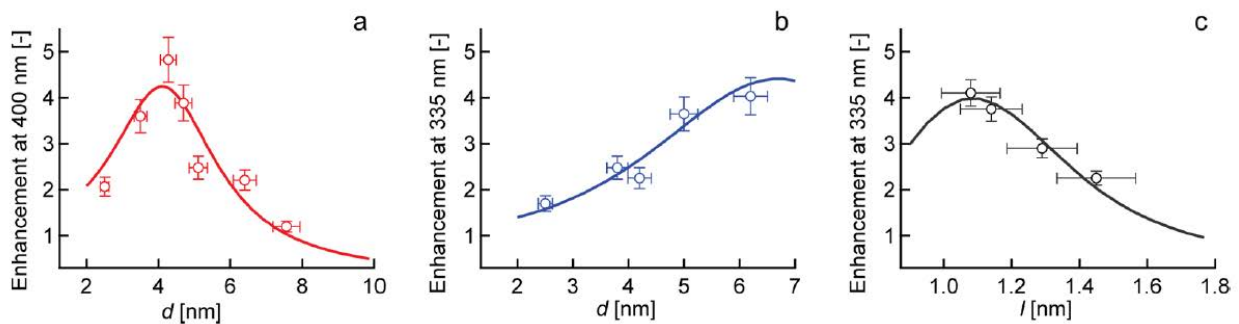
Figure 3.2: Absorption enhancement E for (a) PbS quantum dots stabilized by oleate ligands (l = 1.5 nm) at 400nmas a function of QD diameter d; (b) CdSe quantum dots stabilized by oleate ligands (l = 1.5 nm) at 335 nm as a function of d; and (c) CdSe quantum dots (d = 4.4 nm) as a function of ligand length l, where the respective data points have been obtained using laureate, myristate, palmitate, and oleate ligands.

Figure 3.2(a) and (b) show the absorption enhancement E for PbS and CdSe QDs stabilized by oleate ligands as a function of their diameter at 400 and 335 nm, respectively. For PbS, we find that E initially increases with increasing particle size up to a maximum of 5 at a core size of around 4 nm. For larger sizes, E goes down and reaches values of about 1 for 8 nm particles. In the case of CdSe, E steadily increases within the diameter range studied to level off at a value of around 4 for a diameter of 6.2 nm. We also investigated the influence of the thickness of the ligand shell l. In particular, for a fixed size of CdSe nanocrystal (4.4 nm), the ligand shell was exchanged from oleate to shorter chain carboxylates, including palmitate (C16), myristate (C14) and laureate (C12). Figure 4 represents the enhancement as function the ligand length – as determined from TEM analysis – thus obtained. We find that E steadily decreases from a value of 4 in the case of laureate ligands (l = 1.1 nm) to a value of around 2 for oleate ligands (l = 1.5 nm).

To understand these observation, we see each QD as a polarizable point particle with a polarizability $\alpha_{0,s}$ that depends on its volume, ε_{QD} and ε_h:

$$\alpha_{0,s} = 4\pi\varepsilon_0 r^3 \varepsilon_s \frac{\varepsilon_{QD} - \varepsilon_s}{\varepsilon_{QD} + 2\varepsilon_s} \tag{3.2}$$

The absorption cross section $\sigma_{0,s}$ is then related to the imaginary part of $\alpha_{0,s}$ according to:

$$\sigma_{0,s} = \frac{2\pi}{\lambda n_s} \text{Im}(\alpha_{0,s}) \tag{3.3}$$

Describing QDs as polarizable point particles, the exceptional absorption enhancement in close packed QD monolayers can be intuitively understood by means of dipolar coupling between neighbouring QDs. A polarized QD will induce a polarization field with dominant dipolar character, decaying rapidly outside of the QD. However, opposite from isolated QDs (*e.g.* in a dilute solution), neighbouring QDs in a close packed layer will feel this additional field. Hence, their polarization by an external driving field will be different from that of an isolated QD, which results in a change in absorption cross section. Since the distance $d_{i\,j}$ between two dipoles i and j in a close packed film increases linearly with the QD radius, there is a trade-off in this dipolar coupling: larger particles show a larger polarizability but increased interparticle spacing. Apparently, this gives rise to an optimal separation or, equivalently, an optimal particle size for dipolar coupling, as follows from the experimental data in Figure 3.2.

This qualitative description can be quantified by the coupled dipole (CD) model, which was originally developed to explain collective resonance effects in arrays of metallic particles. Such particles show distinct multipolar plasmon resonances in their single particle polarizability, thus differing fundamentally from the semiconducting QDs studied here. Within this model, we write the local field $E_{L,i}$ polarizing a particular QD i as the sum of the incident external field E and the contribution from the polarization fields of all other QDs j:

$$E_{L,i} = E + \sum_{j \neq i} \beta_{i,j} E_{L,j} \tag{3.4}$$

Here, the coupling coefficients $\beta_{i,j}$ describe the dipole field of QD j at the position of QD i. They are thus proportional to $\alpha_{0,h}/\varepsilon_h$, *i.e.*, the polarizability of an individual QD screened by the host. More importantly, due to symmetry reasons, all QDs must experience the same local field E_L. Thus, we can rewrite eq 3.4 as:

$$E_L = E + \frac{\alpha_{0,h}}{\varepsilon_h} \sum_{j \neq i} S_{i,j} E_L = E + \frac{\alpha_{0,h}}{\varepsilon_h} S E_L \tag{3.5}$$

The quantity S, introduced in eq 3.5 is called the retarded dipole sum. It includes the dipolar contributions from all neighbouring particles to the internal field of the considered particle. A simplified expression for S can obtained by assuming that image charges induced in the substrate are negligible due to its low permittivity, that the center-to-center distance d_{ij} between neighbouring QDs is small compared to the optical wavelength $\lambda = 2\pi/k$ and that the monolayers show only locally hexagonal ordering:

$$S = \sum_{j \neq i} \frac{(1 - kd_{ij})e^{ikd_{ij}}}{8\pi d_{ij}^3} \tag{3.6}$$

Rewriting eq 3.5, we obtain an expression for the field locally driving an individual QD as a function of the incident electric field:

$$E_L = \frac{E}{1 - \dfrac{\alpha_{0,h}}{\varepsilon_h} S} \tag{3.7}$$

Equation 3.7, which describes the local driving field E_L as a function of the incident field E, provides an excellent starting point to understand the occurrence of a maximum enhancement. It indicates that the ratio between E_L and E crucially depends on the product $\alpha_{0,h}S/\varepsilon_h$, *i.e.*, on the combination of the polarizability of an individual QD and the coupling between the QDs. Based on the respective definitions of $\alpha_{0,h}$ and S, it follows that this quantity changes depending on the QD material, the driving frequency (*via* ε_{QD}), the diameter of the QDs and the distance between neighbouring QDs. Assuming for simplicity that $\alpha_{0,h}S/\varepsilon_h$, is a real number, E_L will be enhanced relative to E when $0 < \alpha_{0,h}S/\varepsilon_h < 2$ (see Figure 3.3(a)). Moreover, E_L increases to infinity when $\alpha_{0,h}S/\varepsilon_h = 1$. Returning to eq 5, this actually means that the system of dipoles can support a local driving field without external driving field at the particular driving frequency where this condition holds. Hence, the condition $\alpha_{0,h}S/\varepsilon_h = 1$ determines a resonance condition for the 2D array of coupled, oscillating dipoles. Obviously, we expect that around this resonance condition, the absorbance of the layer will be maximally enhanced, a situation we call optimal coupling. We note that neglecting the imaginary part of the denominator in eq 3.7 is useful for understanding the resonance condition. In reality, the imaginary part limits the increase of E_L, resulting in a damped resonance. For a quantitative comparison between the experimental results and the theory developed here, both the real and imaginary part of S and $\alpha_{0,h}$ are to be taken into account.

In the experiments shown in Figure 3.2, we fix the driving frequency – and thus ε_{QD} – yet we change $\alpha_{0,h}$ *via* the QD size and S *via* both the QD size and the ligand length. To analyze the occurrence of optimal coupling in this case, we rewrite the resonance condition as:

$$\frac{\varepsilon_h \times V_{QD}}{\alpha_{0,h}} = V_{QD} \times S \tag{3.8}$$
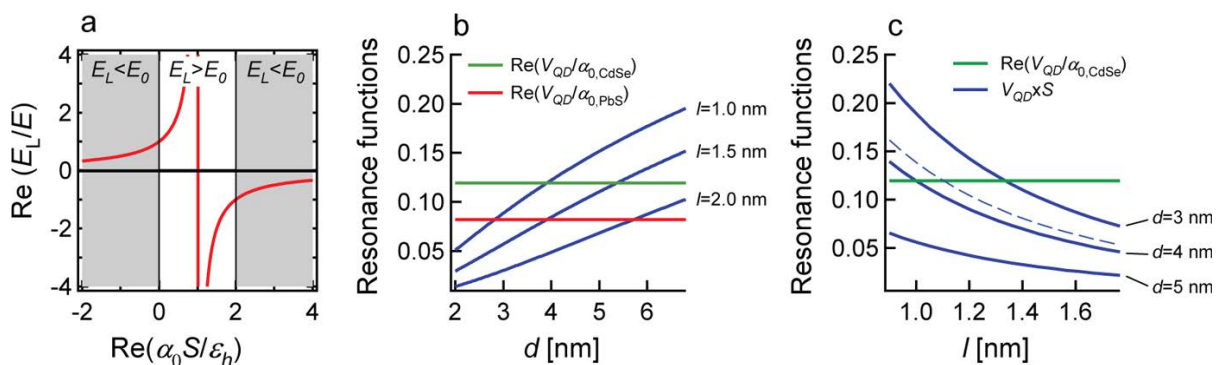
Figure 3.3: (a) Ratio of the local driving field E_L and the external driving field E as a function of the coupling between neighboring QDs as expressed by eq 3.7. (b) Graphical representation of the optimal coupling condition (eq 3.8) showing the term $\varepsilon_h V_{QD}/\alpha_{0,h}$ for (red) PbS QDs at 400 nm and (green) CdSe QDs at 335 nm, together with the term (blue) $V_{QD}S$ for ligand lengths l as indicated as a function of particle size. (c) Same terms plotted as a function of ligand length l for different particle sizes as indicated. In (b) and (c), optimal coupling for a given

material and a given size or ligand length corresponds to the crossing of the respective horizontal and blue lines.
Calculations are done taking ε_h = 1.5 and assuming local hexagonal ordering in the monolayers.

In eq 3.8, the left hand side depends on the QD material and the driving frequency, but not on the QD size or the inter-particle spacing. On the other hand, the right hand side depends on the geometrical parameters of the close-packed layer, i.e., d_{QD} and l. By varying d_{QD} or l, we thus only change $1/(V_{QD} \times S)$, and optimal coupling occurs when eq 3.8 holds. When l = 1:5nm – the experimentally determined ligand shell thickness in the Langmuir-Blodgett films of QDs capped with oleate ligands – Figure 3.3(b) shows that this results in optimal coupling for ≈ 4 nm PbS QDs. This value matches the experimentally observed diameter for maximum enhancement, confirming that the mutual dipolar coupling between adjacent QDs indeed accounts for the observed absorption enhancement. Equation 3.8 and Figure 3.3(b) also show that the lower polarizability of CdSe QDs makes that larger diameters are needed to reach optimal coupling, which is also confirmed experimentally (see Figure 3.2(b)). Also the dependence of the resonance on ligand length can be understood using the resonance condition described in eq 3.8. As plotted in Figure 3.3(c), optimal coupling for 4.4 nm CdSe QDs occurs for a ligand length close to 1.1 nm, which implies a progressive reduction of E for ligand lengths that progressively exceed this value, in line with the experimental data in Figure 3.2(c).

For a more quantitative comparison between our experimental data and the coupled dipole model, we use eq 3.7 to obtain an effective polarizability a film of a QD in a close packed monolayer

$$\alpha_{film} = \frac{\alpha_{0,h}}{1 - \dfrac{\alpha_{0,h}}{\varepsilon_h} S} \tag{3.9}$$

As a result, σ_f and the absorption enhancement read:

$$\sigma_f = \frac{2\pi}{\lambda n_h} \mathrm{Im}\left(\frac{\alpha_{0,h}}{1 - \dfrac{\alpha_{0,h}}{\varepsilon_h} S} \right) \tag{3.10}$$

$$E = \frac{\sigma_f}{\sigma_{0,s}} = \frac{n_s}{n_h} \frac{\mathrm{Im}\left(\dfrac{\alpha_{0,h}}{1 - \dfrac{\alpha_{0,h}}{\varepsilon_h} S} \right)}{\mathrm{Im}(\alpha_{0,s})} \tag{3.11}$$

Equation 3.11 shows that the condition for optimal coupling also controls the enhancement of σ_f. In Figure 3.2, the solid lines represent E for PbS and CdSe QDs, calculated using eq 3.11 at 400 and 335 nm, respectively. As is common for the high energy dielectric function of semiconductor quantum dots, the respective bulk values are used for ε_{QD}. In addition, the film environment is modeled as ε_h = 1.5, which corresponds to an environment of low polarizability. This is a reasonable estimate for an environment consisting of organic ligands, glass and air. Assuming a size dispersion of 10%, we find that the experimental enhancement is in very good

agreement with the enhancement that follows from the assumption of dipolar coupling between neighboring QDs. For both PbS and CdSe, the magnitude and the size-dependence of E are correctly predicted with, for the particular example of PbS, a maximum enhancement for a diameter of around 4 nm. Also, for CdSe, the dependence of E on the ligand length l is well reproduced.
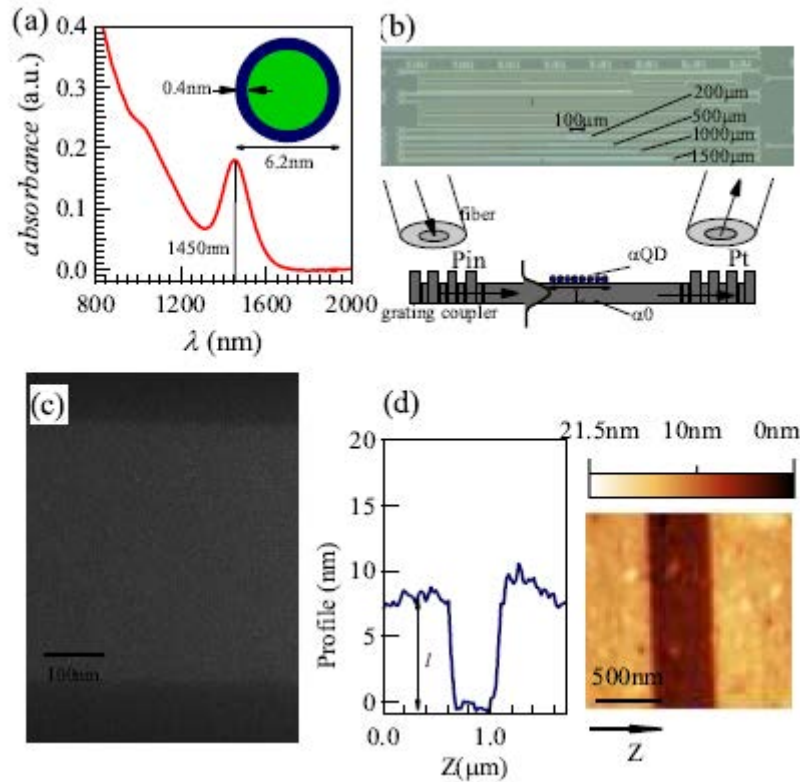

3.2. Optical properties of quantum dot functionalized SOI waveguides

In device applications, colloidal QDs are mostly deposited as close packed nanocrystal thin films, either within a layered stack or as a surface coating where they interact with the internal or evanescent optical field, respectively. A typical example here involves QDs embedded in a resonator, where the coupling of the QD light emission to the resonator modes eventually leads to lasing. Essential to the development and optimization of such QD-based devices is a proper understanding of the optical field in materials with embedded or surface-coated QD films, where the influence of the QD film on the optical field is properly taken into account. In the literature, it is well known that a dilute dispersion of QDs, either in a liquid or a solid host, can be described as an effective optical medium according to the Maxwell-Garnett effective medium theory in the local field approximation. On the other hand, far less studies have addressed the effective medium description of close packed QD films, let alone the experimental investigation and theoretical simulation of the optical properties of hybrid materials containing close packed QD films.

We analyze the absorption coefficient of SOI planarized waveguides (PWGs) coated with close packed mono- and multilayers – generally denoted as i-layer with i = 1, 2, ... – of PbS/CdS QDs. We retrieve the fingerprint of the QDs in the waveguide absorbance and find that the absorbance per QD increases with the number of QD layers. The experimental data are compared with simulation results, where the QD i-layers are described as an effective medium in which the optical properties depend on dipolar coupling between neighbouring QDs. Close agreement between the experimental values and the simulation results is obtained using the dielectric constant ε_h of the QD host material as the only adjustable parameter. We find that the increased absorbance in thicker layers makes that a higher value of ε_h is needed to match the simulated and the experimental data. We interpret this as a transition from a regime where the field lines coupling the QDs mainly pass through the surroundings (monolayer case) to a situation where these field lines are mainly confined within the QD stack (thicker multilayers).

The PbS/CdS core/shell QDs used in this work were synthesized using an established cationic exchange procedure [21]. Core diameter and shell thickness were adjusted to have band gap absorption at 1450 nm (see Fig. 3.4a). In this way, the long wavelength side of the absorption peak covers the 1500 − 1550 nm bandpass window of the SOI grating couplers, which are used to couple light in and out of the waveguides. This will make the QD absorption well discernible in the measurements. Using the absorption spectrum of the original PbS QDs and the resulting PbS/CdS QDs, core diameter and shell thickness were estimated to be 5.4 and 0.4 nm, respectively.

The QDs were locally deposited on the PWGs by combining optical lithography and Langmuir-Blodgett deposition, forming strips of 200, 500, 1000, 1500 μm on otherwise identical waveguides. The scanning electron microscopy image shown in Fig. 3.4c is indicative of the close packing and locally hexagonal ordering of the QDs on top of the PWG, while atomic force microscopy imaging reveals that the PWGs are depressed by 5 − 10 nm relative to the surrounding silica, with the QD layer conformally following this geometry (see Fig. 3.4d).

FP7-ICT-2011-7
Project-No. **288869**
NAVOLCHI – D4.2

Deliverable Report
Last update 01/31/2012
Version 1

Figure 3.4: (a) Absorption spectrum of the PbS/CdS QD used here, as recorded on a dilute QD dispersion in tetrachloroethylene. (b) Optical microscopy image of a sample with planarized waveguides coated by a QD monolayer with various strip lengths and a cartoon representation of the opitcal field coupled from the fiber through the grating in the QD coated PWG. (c) Scanning electron microscopy image of a (topview) PWG coated by a QD monolayer. The resolution is such that the individual QDs coating the waveguide can be discerned. (d) Atomic force microscopy image and cross section of a PWG coated by a QD monolayer, clearly showing the offset (l) between the top surface of the (slightly submerged) PWG and its silica cladding.

The use of QD stripes with different interaction length on identical waveguides enables us to quantify the light absorption in the QD functionalized sections of the PWGs, regardless of coupling losses (see Fig. 3.4b). Indeed, denoting the absorption coefficient of a bare and QD coated PWG α_0 and α, respectively, the net absorption coefficient $\alpha_{QD=}\ \alpha-\alpha_0$ of a QD coated PWG can be derived from the transmitted power P_t through PWGs with different QD strip lengths L. More specifically, using the length of and the power transmitted through one of the QD coated waveguides as a reference, the net waveguide absorbance A reads:

$$A = \log \frac{P_{t,ref}}{P_t} = (\alpha - \alpha_0)(L - L_{ref}) \tag{3.12}$$

According to eq. 3.12, α_{QD} can be obtained from a plot of A versus the strip length difference $\Delta L = L-L_{ref}$. This is exemplified by Fig. 3.5a, which shows A as obtained from measurements on a PWG coated by a PbS/CdS QD 2-layer using the 200 μm strip as a reference. Clearly, A is proportional to ΔL and α_{QD}, and can thus be obtained as the slope of the best fitting line passing through the origin. The difference between the absorption coefficient thus obtained – 6.6(3) cm^{-1} – and the determined 1.8 dB/cm (i.e., 0.41 cm^{-1}) loss of an uncoated PWG provides a first

indication that the QD coating has a strong influence on the waveguide absorbance. This conclusion is further supported by the wavelength dependence of α_{QD}.
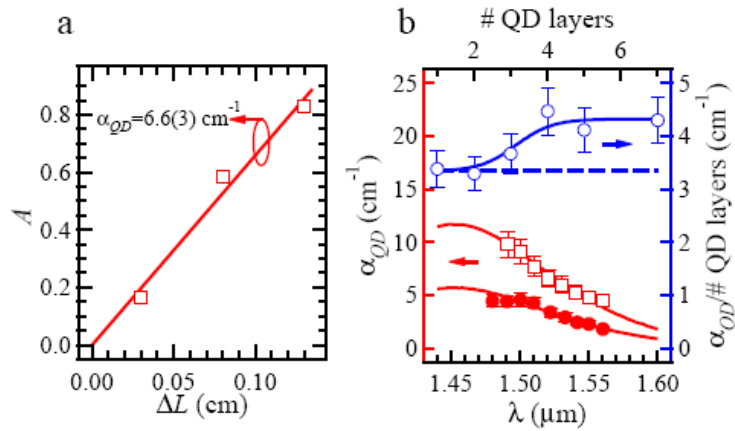
Figure 3.5: (a) (open squares) Absorbance A – as defined by eq. 3.12 – at 1520 nm as a function of the strip length difference ΔL for PWG coated with a PbS/CdS QD 2-layer strip 500, 1000, and 1500 μm long using the power transmitted through a similar waveguide with a 200 μm QD 2-layer as a reference and (full line) best fit of the data to a line passing through the origin with an indication of the thus obtained absorption coefficient α_{QD}. (b) (red, left and bottom axis) α_{QD} thus determined as a function of wavelength for a (filled circles) QD monolayer and a (open squares) QD 2-layer coated PWG. The full lines represent the absorption spectrum of dispersed PbS/CdS QDs normalized to match the respectively measured absorption coefficients. (blue, right and top axis) α_{QD} per QD layer at 1520 nm. The full line is a guide to the eye and the dashed line indicates the average value obtained for a monolayer and a 2-layer.

As shown in Fig. 3.5b, the α_{QD} spectrum for a mono- and a 2-layer coating strongly resembles the absorption spectrum of the PbS/CdS QDs used in a dilute tetrachloroethylene dispersion. Similar results are obtained using films consisting of up to 7-layers. Remarkably, we find a higher absorption coefficient per layer for thicker layers (see Fig. 3.5b), meaning that the absorption cross section of a QD in, e.g, a 7-layer is larger than in a monolayer.

To compare the experimental α_{QD} with model predictions, we use an approach where the real QD i-layer covering the PWG is replaced by an effective medium with a dielectric function ε_{eff} (see Fig. 3.6a). Using the real geometry of the PWG – including the slightly submerged waveguide top surface, coated by a thin native silica layer – this enables us to extract a theoretical absorption coefficient $\alpha_{QD,th}$ from the simulated effective refractive index $n_{eff,c} = n_{eff} + i\kappa_{eff}$ of the propagating quasi-TE mode:

$$\alpha_{QD,th} = \frac{4\pi\kappa_{eff}}{\lambda} \tag{3.13}$$

This approach however requires that the dielectric function of each material or medium involved is known. For silicon and silica, we use typical values at 1520 nm of 3.45 and 1.45, respectively.

For ε_{eff}, we build on the finding in the previous section that the absorption cross section of QDs in close packed monolayers is similar to the ones used here and can be well described by taking dipolar coupling between neighbouring QDs explicitly into account. We also show that the coupled dipole model (CDM) applies to all PbS/CdS QD i-layers used in this study. Moreover, it can be extended to yield an expression for ε_{eff}:

$$\varepsilon_{eff} = \varepsilon_h \left(\varepsilon_0 + \frac{N_s}{L_t} \frac{a_{QD}}{1 - a_{QD}S} \right) \tag{3.14}$$

Here, N_s is the QD surface density in the layer, L_t is the thickness of the effective layer, a_{QD} is the polarizability of a single PbS/CdS QD and S is the dipole sum, which sums up the influence of the dipolar field of neighboring QDs on an individual QD in the layer. In general, S is different for fields parallel ($S_\parallel$) or perpendicular ($S_\perp$) to the QD film. However, since the main field component of the quasi-TE modes in the PWG used here lies parallel to the QD film, only $S_\parallel$ – which was analysed experimentally in the previous section (eq. 3.6) – is of relevance here.

Opposite from S, which only depends on the position of the particles relative to each other, a_{QD} is a function of ε_h and the dielectric function $\varepsilon_{QD} = \varepsilon_{QD,R} + i\varepsilon_{QD,I}$ of the QDs. While we consider ε_h as an adjustable parameter in this study, we use calculated values for $\varepsilon_{QD,R}$ and $\varepsilon_{QD,I}$, taking care that they yield the experimental absorption coefficient spectrum of the QDs in a dilute dispersion while obeying the Kramers-Kronig transformation. [22] Importantly, in this analysis, we assume that the absorption coefficient of the PbS/CdS core/shell QDs at wavelengths shorter than 400 nm can be derived from the bulk dielectric function of PbS and CdS, respectively – as was demonstrated for PbSe/CdSe QDs[m] – and we neglect possible quantization effects in the CdS shell.
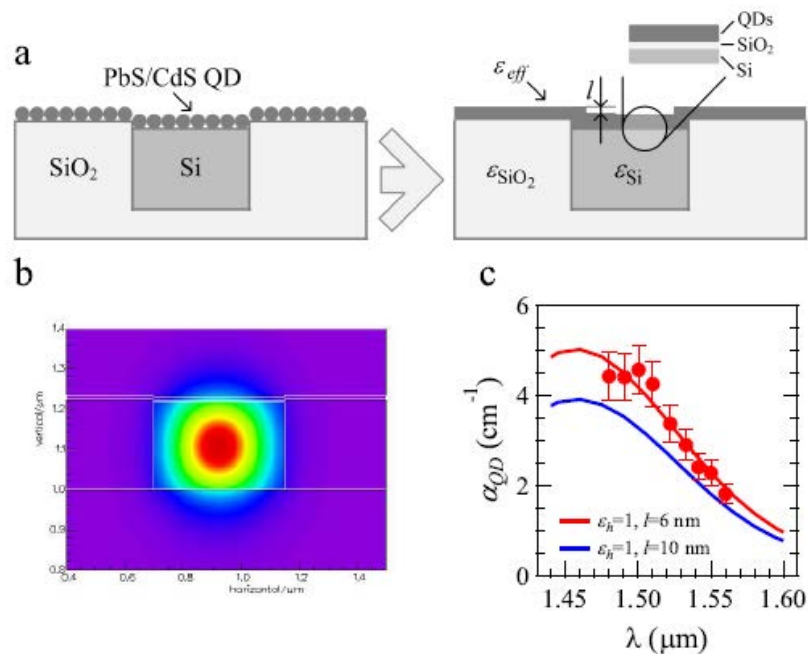
Figure 3.6: (a) Cartoon representation of the replacement of the real QD film on top of an SOI planarized waveguide by an effective medium. Indicated are the height difference l between the top surface of the PWG and its silica cladding and the native silica layer in between the PWG top surface and the effective medium representing the QD film. (b) Cross-sectional representation of the simulated electric field for 1520 nm light guided by a PWG coated by a QD monolayer. (c) Comparison of the experimental and simulated α_{QD} absorbance spectrum of a QD coated PWG for two different combinations of l and ε_h.

Combining the geometry of the PWG cross section and the expression for ε_{eff} – based on the coupled dipole model and the self-consistently determined ε_{QD} – the electric field of the guided optical mode in the PWG can be calculated, resulting in theoretical values for $n_{eff,c}$ and $\alpha_{QD,th}$. As an example, Fig. 3.6b represents the electric field at a wavelength of 1520 nm for a PWG covered by a QD monolayer as obtained using Fimmwave 3.4 complex mode solver. The figure

FP7-ICT-2011-7   **Deliverable Report**
Project-No. **288869**   Last update 01/31/2012
NAVOLCHI – D4.2   Version 1

clearly shows the overlap between the QD film and the evanescent field, which makes that light absorption by the QDs affects ε_{eff} and leads to a non-zero $\alpha_{QD,th}$. As shown in Fig. 3.6c, a close match can be obtained between the simulated and experimental α_{QD} spectrum for a QD monolayer-coated PWG by adjusting ε_h. It should be noted that the ε_h value needed to match the experimental and simulated _QD somewhat depends on the geometry of the PWG. Looking at the AFM cross section of the PWG (see Fig. 3.6d), an exact value of the height difference l between the top surface of the PWG and its silica cladding is hard to determine. Varying l between 6 and 10 nm as extreme cases, we obtain agreement between experiment and simulation for $\varepsilon_h = 1.0$ ($l = 6$ nm) to $\varepsilon_h = 1.16$ ($l = 10$ nm). For QDs capped by oleic acid ($\varepsilon_h = 2.1$ at 2000 nm), both figures are relatively low yet they agree with the $\varepsilon_h = 1.0$ found for PbS and CdSe QD monolayers deposited on glass.
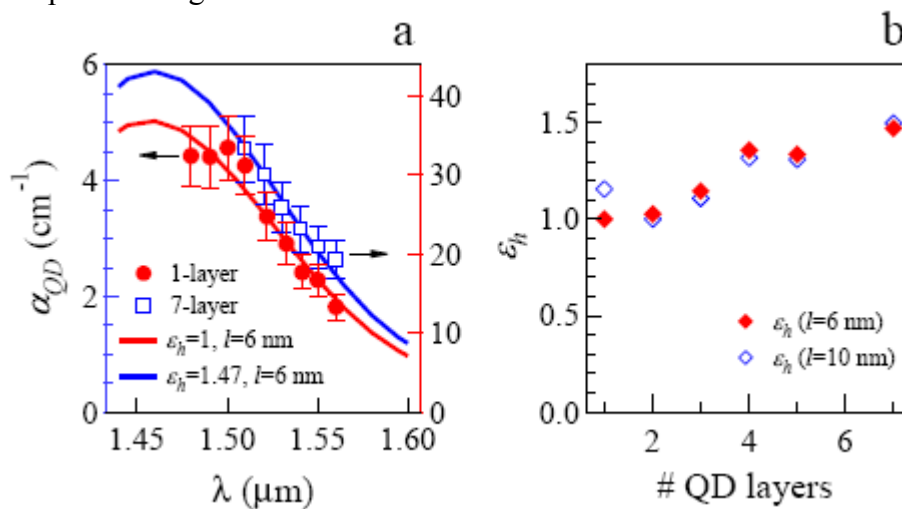
Figure 3.7: (a) Comparison of the experimental and simulated α_{QD} spectrum of a PWG coated with (blue) a QD mono- layer and (red) a QD seven layer. The respective axis are scaled by a factor of 7 to allow for a direct comparison of the absorbance per number of layers. (b) Evolution of ε_h values needed to match experimental and simulated absorption coefficient calculated for the extreme case of (red) $l = 6$ and (blue) $l = 10$ nm. (c) The experimental absorption coefficient at 1520 nm shows stronger absorption than expected from simulating α_{QD} for $\varepsilon_h = 1$, $l = 10$ nm.

The approach as outlined above can be readily extended to simulate α_{QD} for PWG covered by QD i-layers. Using once more ε_h as an adjustable parameter, correspondence between experimental and simulated values can be obtained as shown by the example of a 7-layer in Fig. 3.7. Importantly, the increasing QD absorption cross section with thicker layers makes that a larger ε_h is needed to fit the simulations to the experimental data when the number of layers increases. As shown in Fig. 9b, an ε_h in the range of 1.00-1.16 is obtained in the case of a monolayer, whereas values between 1.47 and 1.50 are found for the simulation of the 7-layer using $l = 6$ and $l = 10$ nm, respectively. This demonstrates that in the case of a QD i-layer with i close to one, ε_h is not an intrinsic property of the QD film. Since the field lines that couple neighbouring QDs in a monolayer mainly pass through the surroundings, the combined effect of the layers surrounding the QDs – air and native silica on silicon– and the organic ligands separating the QDs will determine ε_h in this case. For thicker layers however, the larger part of these coupling fields remains within the QD film. In that respect, the trend shown in Fig. 3.7b can be interpreted as the progressive evolution of ε_h from an extrinsic value, determined by the layer and its surroundings, in the monolayer case to a value that is an intrinsic property of a QD multilayer.

4. Nanocomposites for optical amplification

4.1. Fabrication of the nanocomposite

Colloidal QDs and quantum nanostructures described in section 2 were dispersed in PMMA and SU-8 polymers to develop nanocomposites able to provide gain in a plasmonic waveguide.

PMMA is a suitable polymer for integrated optics applications due to its trouble-free process and high transparency. Figure 4.1.a compares the transmittance of PMMA with that of the glass substrate where they are deposited by spin-coating. Clearly the layers exhibit a transparency higher than 90 % between 400 and 1500 nm [6]. Then, this polymer becomes an interesting material for waveguiding applications when it is deposited on a low index wafer (in this case SiO$_2$/Si). Moreover, PMMA is an appropriate host polymer for embedding oleate-capped QDs due to their adequate chemical interaction. In this way, homogenous films can be obtained, which suggests a great potentiality of these nanocomposites for photonic applications. Most of the results obtained with PMMA incorporating different QDs and nanostructures are summarized below.
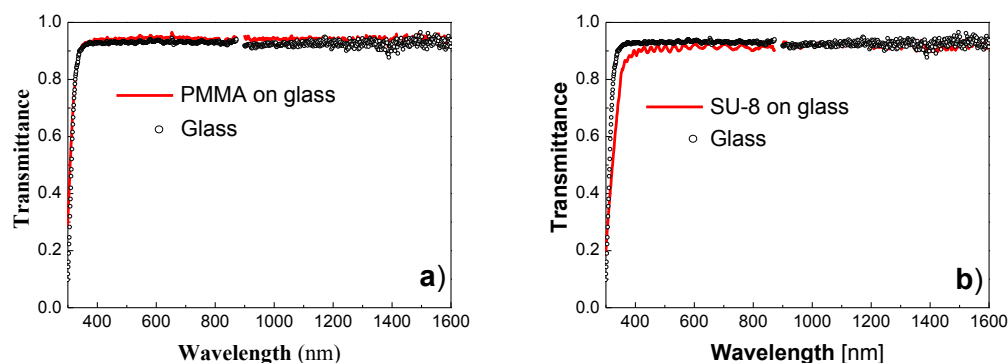

Figure 4.1: Transmittance of PMMA (a) and SU-8 (b) on a glass substrate.

PMMA is commonly used to develop nano/micropatterns by means of e-beam lithography. However, this patterning technique is highly time consuming and expensive as compared to UV-photolithography to fabricate photonic devices on the whole wafer. For this reason, SU-8 photoresist was selected as a promising material for developing different photonic elements of the final chip. In fact, this material is one of the most used for polymer based wave-guiding applications [23], because it is easily patternable by UV photolithography and has a high refractive index (around 1.5108 at 600 nm) [24]. Figure 4.1.b shows the transmittance spectrum of a SU-8 film spin coated on a glass substrate. Between 600 and 1500 nm the transmittance is very similar to that of the bare glass, but below 600 nm the absorption increases due to its sensitivity to the UV radiation. As a result, SU-8 is an ideal candidate for hosting QDs, even if the main drawback lies in the poor chemical compatibility with as-syntesized QDs. The SU-8 photoresist is normally formulated with γ- butyrolactone or cyclopentanone, where oleate-capped QDs are not soluble. It is well known that surface modification of QDs may result in a change in the solubility properties of QDs [25]. In this way we propose a ligand exchange on oleate-terminated QDs to enhance their solubility in, γ–butyrolactone [26].

For the fabrication of the nanocomposites, the QD colloidal solutions are mixed with that of the polymers under appropriate dilution to obtain a filling factor (volume ratio of QDs in the

matrix) of around 10^{-3}, which is found to optimize the waveguiding conditions [6]. Then, nanocomposites are deposited on the substrate by spin coating and baked at the necessary temperatures to evaporate the solvent and polymerize the layer. If PMMA is chosen as a matrix the resulting film is heated at 80 and 150 ºC during two minutes each. In the case of SU-8 it was followed the process recommended for this resist [24]; it suffers two bakes at 65 and 95 ºC during two minutes each after spin coating on the wafer. Then, the film is exposed to a UV lithography using a mask consisted in consecutive sets of lines of widths (w) 4, 6, 8, 10 and 20 μm with a gap of 50 μm between the lines and 100 μm among the sets. After illumination, the films were subjected to post-bakes of 65 ºC and 95 ºC for two minutes each. Finally, they were developed during one minute until SU-8 ridges patterns became defined. The thicknesses of the PMMA and SU-8 films were varied between 0.5 and 3 μm by controlling the spin-coating speed and the quantity of solvent in the solution.

Preliminary results of waveguiding using QDs emitting in the visible, as background for Navolchi, were firstly published in Refs. 6 (in PMMA), 27 (in PMMA and SU-) and 28. In Ref. 16 the work included the evaluation of gain and losses of propagating light emitted by QDs and the application to disperse several QD materials in appropriate proportions. A more recent work using these QDs, but now proposing more efficient designs for waveguided light was recently submitted for publication [29]; these structures consisted of an active PMM-QD active layer cladded by either PMMA (constituting a planar waveguide) or SU-8 (to pattern linear waveguides) were modeled by finite differences incorporating carrier/photon generation and propagation, fabricated and characterized. These results are summarized below, together with those obtained by using quantum nanostructures emitting at infrared wavelengths.

a. *Refractive index*

The effective refractive index of the QD-polymer can be calculated using Bruggeman's approximation:

$$(1 - \text{ff}) \cdot \frac{n_{pol}^2 - n_{\text{eff}}^2}{n_{pol}^2 + 2 \cdot n_{\text{eff}}^2} + \text{ff} \cdot \frac{n_{QD}^2 - n_{\text{eff}}^2}{n_{QD}^2 + 2 \cdot n_{\text{eff}}^2} = 0 \tag{4.1}$$

where *ff* is the filling factor of QDs, n_{QD} the refractive index of the nanostructures and n_{pol} the refractive index of the polymer. Then, the refractive index of the nanocomposite is larger than the one of the polymer because of the influence of the nanoparticles. Also, although the polymers have transparency in the region of interest, the nanocomposite will exhibit absorption proportional to that of QDs and hence increasing with increasing *ff*. As an example table I shows effective refractive indexes deduced in [6] for CdSe-PMMA waveguides. For this purpose the dispersion curve of the real part of n_{QD} (*n′*) has been fixed to that of bulk CdSe. The imaginary part (*n″*) depends on the specific size of the QD, and it is assumed to have a wavelength variation given by the experimental curve of the QD colloid. Figure 4.2 shows the reflectivity obtained when the nanocomposites were deposited on a SiO_2/Si substrate. Symbols correspond to the experimental data and red straight lines to the effective refractive index estimated by Eq. 4.1 (values listed in table I for different *ff*). For a filling factor smaller than 10^{-3} the real part of the effective refractive index can be approximated to the one of the polymer, but its imaginary part is different than zero and proportional to the absorption coefficient of the QDs, as deduced from the original colloids (see section 2), for example.

FP7-ICT-2011-7
Project-No. **288869**
NAVOLCHI – D4.2

Deliverable Report
Last update 01/31/2012
Version 1

Table I Effective refractive indexes and PL peak in CdSe-PMMA nanocomposites

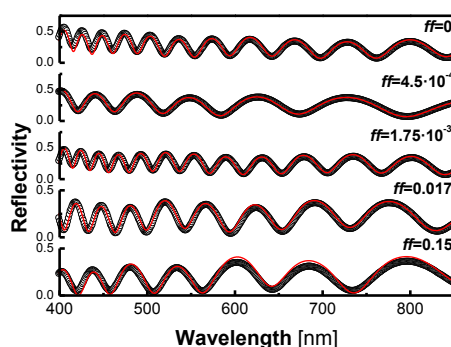| Filling factor	n_{eff}	PL peak (nm)
0.15	$1.65022- 0.02 \cdot i$	610
0.017	$1.50618-0.002 \cdot i$	610
$1.75 \cdot 10^{-3}$	$1.49101-10^{-4} \cdot i$	610
$4.5 \cdot 10^{-4}$	$1.48945-9 \cdot 10^{-5} \cdot i$	600
0	1.489	-

Figure 4.2. Reflectivity curves of CdSe-PMMA nanocomposites ona SiO2/Si substrate. Symbols correspond to the experimental data and red lines to the modeling [6].

b. PL and absorption properties of QD-nanocomposites

The absorption spectrum of a QD-nanocomposite has a similar wavelength variation proportional to the concentration of the quantum nanostructures. Concerning the PL properties, the PL peak can be shifted depending on the concentration due to the fact that high proportion of QDs tends to agglomerate increasing the effective size of the particles and hence the effective band gap. Table I showed the PL peak in CdSe-PMMA nanocomposites with different concentrations. For the case of *ff* used in waveguiding applications ($\sim 10^{-3}$) PL peak is blue-shifted 10 - 20 nm with respect to the value measured in the colloidal solution.

c. Waveguiding

Active dielectric waveguides were fabricated by depositing the nanocomposite on a SiO$_2$/Si substrate. The wafers were supplied by CEMAT and consisted of 2 μm SiO$_2$ grown on a silicon substrate. Given that the refractive index of SiO$_2$ (n~1.45) is smaller than the one of the polymer (n~1.5) the nanocomposite will act as the core of an active waveguide and its propagation properties will depend strongly on the nanoparticle chosen and its concentration in the polymer matrix. In Ref. 6 the optimum concentrations of QDs in PMMA were obtained for waveguiding. For high filling factor ($>10^{-2}$) the roughness and the attenuation is too high to allow the propagation at any wavelength. Nevertheless, as long as the concentration is reduced light can start to propagate and samples characterized by end fire coupling of the pumping laser on one of the film edges and collecting the waveguided PL light on the opposite edge (experimental set-up

FP7-ICT-2011-7
Project-No. **288869**
NAVOLCHI – D4.2

Deliverable Report
Last update 01/31/2012
Version 1

shown in figure 4.3.a). On the opposite, if $ff < 10^{-3}$ the waveguiding is possible for wavelengths shorter (405 or 532 nm lasers, for example) and longer (PL) than that of the absorption edge. However, for gain applications the filling factor should be increased to values in the range 10^{-2}-10^{-3} were the nanocomposite films can only waveguide the PL, but not the pump beam. Alternatively, it is possible to pump the waveguides from the top surface using the set-up shown in Figure 4.3.b. In order to limit the influence of the Gaussian shape of the laser beam a slit after the spot line was placed and kept the central 1.4 mm of the line produced by the focusing cylindrical lens. The pump power is constant along the length of the pump line and hence the QDs are excited homogeneously. Now reabsorption and roughness effects will be the main factors limiting the propagation of PL, even if the first can be reduced by incorporating quantum nanostructures with large Stokes shift (semiconductor nanorods described in section 2). The propagation of PL signal in waveguides follows the equation:

$$\frac{dI_v(x)}{dx} = I_{SS} + (g - \alpha) \cdot I_v(x) \tag{4.2}$$

where I_v is the intensity of the light, I_{SS} the intensity of the spontaneous emisison, g the gain and α the losses. Then, gain of the structure can be estimated by measuring the emission as a function of the strip length (d) by the variable stripe length (VSL) method [30]. As long as the nanocomposite is more concentrated the intensity growth (its slope determines the gain) becomes sharper. If gain was a constant factor the waveguided intensity increases as:

$$I(d) = \frac{I_{SS}}{g - \alpha} \cdot \left(e^{(g-\alpha) \cdot d} - 1 \right) \tag{4.3}$$

However, this is not the case, where a gain saturation function due to Auger non-radiative recombination should be included in Eq. 4.3 to give account of the experimental results [31]:

$$g = g_0 \cdot e^{-d/L} \tag{4.4}$$

where g_0 and L are fitting parameters related to gain and saturation length, respectively. In the same way, keeping the length of the stripe constant and moving it away from the edge of the sample we directly measure the attenuation constant α of propagating light in the waveguide. Then, propagation losses can be fitted by approximating the dependence of the output intensity as a function of the distance between the stripe and the edge of the sample (x) with an exponential decrease:

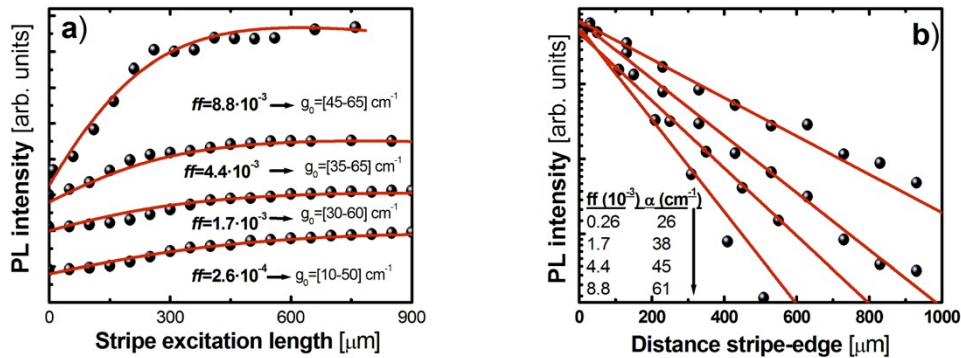$$I(x) \propto e^{-\alpha \cdot x} \tag{4.5}$$
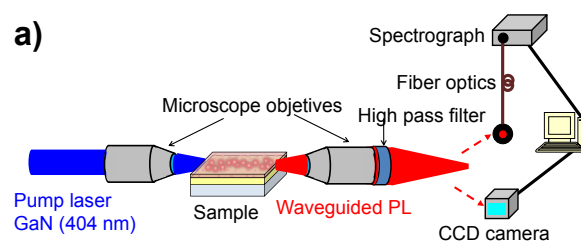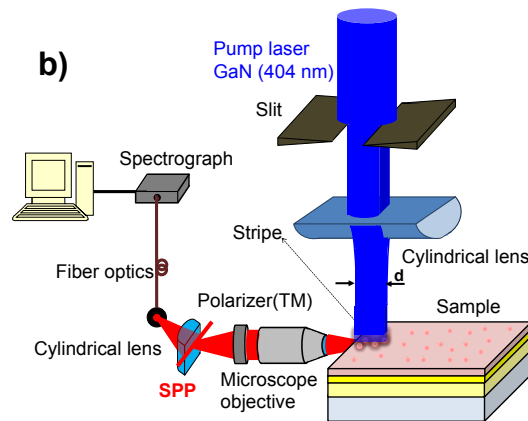
Figure 4.3. Experimental set up to couple light from the edge of the sample (a) and laser pumping from the top surface

## 4.2.   Gain and losses in QD-nanocomposite waveguides

a. CdSe-PMMA

Figure 4.4 shows the VSL results obtained on CdSe-PMMA waveguides with different concentrations of CdSe in PMMA (*ff* $=2.6·10^{-4}, 1.7·10^{-3}, 4.4·10^{-3}$ *and* $8.8·10^{-3}$). Figure 4.4.a plots the PL intensity as a function of the stripe excitation length; symbols correspond to the experimental data and red straight lines to the modelling using Eqs. (1-3). The signal increases significantly with the length of the stripe and reaches saturation for lengths between 300 and 900 µm, depending on the concentration. The model fits well the experimental data by setting L between 200 and 250 µm (these values are similar for all materials and will be fixed in all fits) and values of g_0 for different *ff* are given in the plot. The value of g_0 obtained from the best fit tends to increase with *ff* due to the growing amount of QD absorbers/emitters. However, the propagation losses also increase in the same proportion due to reabsorption effects [28]. Figure 4.4.b shows the dependence of the PL intensity as a function of the distance between the stripe and the edge of the sample (keeping the strip length constant) in the four samples studied in Figure 4.4.a; the losses increases from 26 to 61 cm^{-1} from the lowest to the highest *ff*. In all cases losses are similar or bigger than g_0 and hence net gain is not reached. A first strategy to solve this issue is the use of other semiconductor nanostructures with larger Stokes shift than spherical QDs in order to reduce reabsorption effects along the propagation of the PL signal beam, as corroborated below by using semiconductor nanorods.

FP7-ICT-2011-7
Project-No. **288869**
NAVOLCHI – D4.2

Deliverable Report
Last update 01/31/2012
Version 1

Figure 4.4: VSL method applied to the characterization of gain and losses in CdSe-PMMA dielectric waveguides: (a) PL intensity as a function of the stripe excitation length and (b) PL intensity as a function of the distance between the stripe and the edge of the sample. The detection wavelength is that of the PL peak (570-590 nm, depending on *ff*).
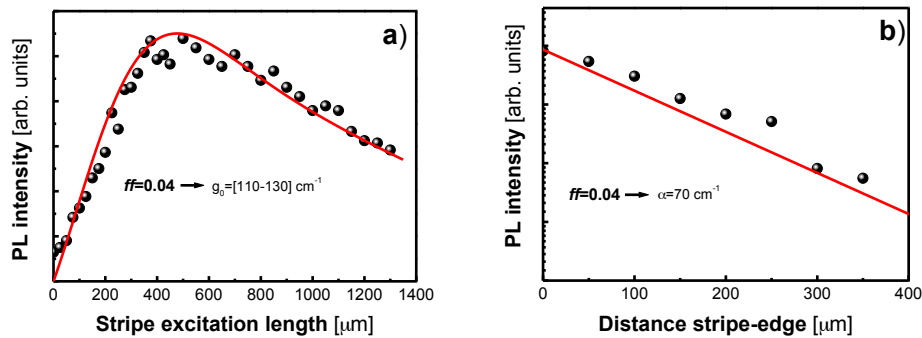
b. PbS-PMMA

Figure 4.5 shows the application of the VSL method to waveguides made by dispersing spherical core-QDs of PbS emitting at the infrared (described in section 2d) in PMMA using an intermediate concentration of *ff* = 0.04. The best fitting values for g_0 ranged between 60 and 80 cm^{-1} (Fig. 3.5.a), but again the losses (Fig. 3.5.b) are more important (90 cm^{-1}), preventing amplification, as occur for CdSe QDs emitting at visible wavelengths.
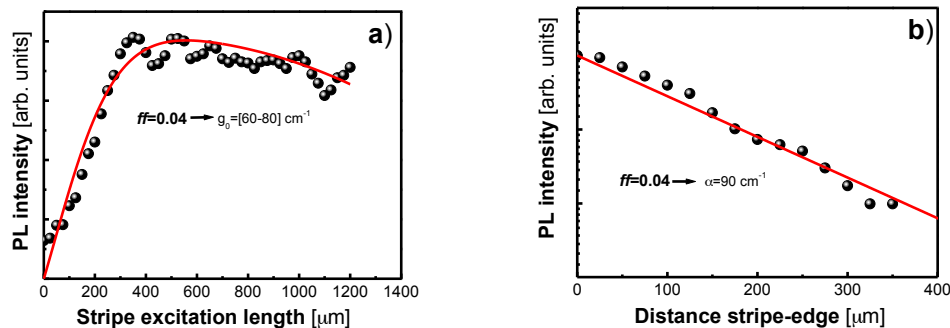
Figure 4.5: VSL method applied to the characterization of gain and losses in PbS-PMMA dielectric waveguides: (a) PL intensity as a function of the stripe excitation length and (b) PL intensity as a function of the distance between the stripe and the edge of the sample. The detection wavelength is that of the PL peak (≈1500 nm).

c. PbS/CdS PMMA

Figure 4.6 shows the application of the VSL method to waveguides in a waveguide made by the dispersion of PbS/CdS semiconductor nanorods (section 2f) in PMMA with *ff=0.04*. In this case g_0 reaches a value around 120 cm^{-1}, slightly larger than that found above for spherical core-QDs (in PMMA nanocomposites with the same *ff*), whereas losses reduce to 70 cm^{-1}. Therefore, one could say that net gain could be possible in waveguides fabricated with this kind of nanostructures if their length is shorter than 400 μm, before the observed intensity saturation in Fig. 4.6.a. This means that our previous hypothesis of reducing reabsorption losses by using semiconductor nanoparticles with larger Stokes-shift was correct.

FP7-ICT-2011-7
Project-No. **288869**
NAVOLCHI – D4.2

Deliverable Report
Last update 01/31/2012
Version 1

Figure 4.6: VSL method applied to the characterization of gain and losses in PbS/CdS-PMMA dielectric waveguides: (a) PL intensity as a function of the stripe excitation length and (b) PL intensity as a function of the distance between the stripe and the edge of the sample. The detection wavelength is that of the PL peak ($\approx$1400 nm).

d. PER-PMMA

Figure 4.7 shows shows the VSL results obtained on PMMA waveguides containing PER nanorods (section 2g); two different *ff* values were used, 0.01 and 0.06. In the sample with the highest concentration of semiconductor nanostrutures g_0 can reach values up to 370 cm^{-1} with losses limited to 100 cm^{-1}. Again, net gain and amplification would be possible with this kind of nanoparticles within a waveguide length shorter than 250 μm. In the sample with *ff=0.01* the gain is much lower and closer to the losses factor (~16 cm^{-1}). We can also say that attained maximum PL intensity and corresponding gain increases slightly non linear (10 times) with the nanoparticle concentration in the PMMA-nanocomposite (6 times), whereas losses increase in a similar amount, as expected.
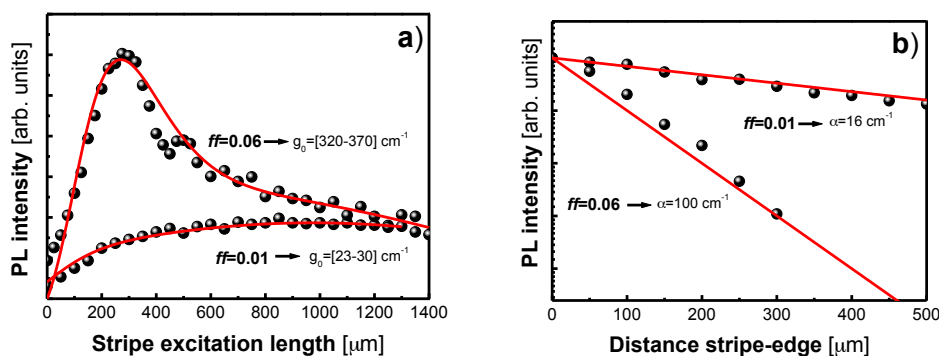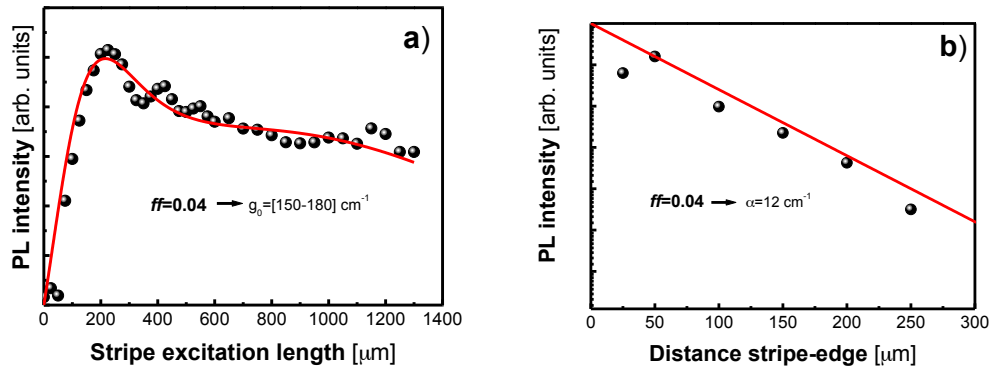

Figure 4.7: VSL method applied to the characterization of gain and losses in PER-PMMA dielectric waveguides: (a) PL intensity as a function of the stripe excitation length and (b) PL intensity as a function of the distance between the stripe and the edge of the sample. The detection wavelength is that of the PL peak ($\approx$1100 nm).

e. PbS/CdSe-PMMA

Figure 4.8 shows the VSL results obtained in a waveguide made by dispersing PbS/CdSe nanorods (section 2h) in PMMA with *ff =0.04*. The best fitting value for case g_0 reaches a value above 150 cm^{-1}, very similar to the case of PbS/CdS nanorods, but for a maximum waveguide

length of around 200 μm. Again, the large Stokes shift in these nanostructures yields a g_0 value higher than the losses factor (12 cm^{-1}). The main difference between both kind of nanorods, CdS versus CdSe shell materials, can lie in the band alignment between shell and core materials, introducing different confinement conditions for electron and holes and hence influencing the excitonic transition and Auger recombination rates.

Figure 4.8: VSL method applied to the characterization of gain and losses in PbS/CdS-PMMA dielectric waveguides: (a) PL intensity as a function of the stripe excitation length and (b) PL intensity as a function of the distance between the stripe and the edge of the sample. The detection wavelength is that of the PL peak (≈1300 nm).

f. SU-8 nanocomposites

As argued above, lithographic properties and high transparency in the visible and IR regions of SU-8 are important properties for the fabrication of passive, but also for active photonic devices by incorporating QDs, once solved the problem of QD solubility in the SU-8 photoresist, as discussed in previous section. Figure 4.9 shows preliminary results of PL waveguiding in patterned bidimensional ridge waveguides using SU-8 nanocomposites with CdSe (Fig. 4.9.a) and PbS (Fig. 4.9.b) QDs, together with the optical mode distributions for different waveguide widths (insets in Fig. 4.9). It should be mentioned that UV-photolithographic performance of SU-8 was not disturbed by the presence of QDs. The concentration of QDs in SU-8 was low enough to consider any remarkable refractive index increase of the matrix as obtained in PMMA nanocomposites.
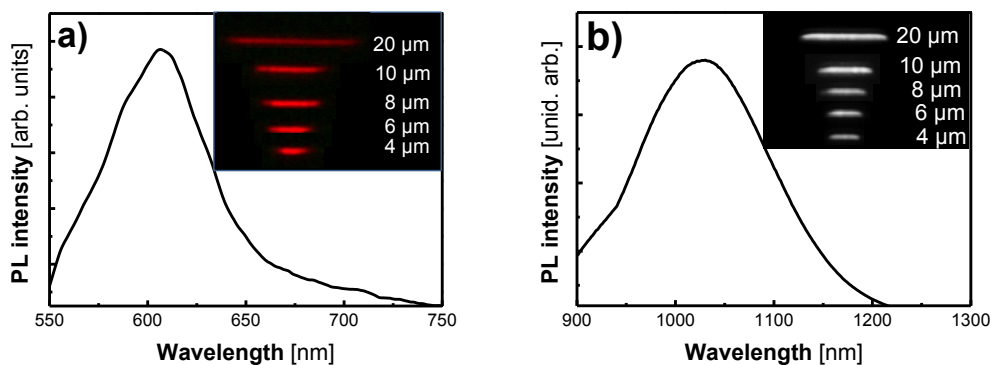
Figure 4.9: PL waveguided spectra based on CdSe/SU-8 (a) and PbS/SU-8 (b) nanocomposites. The inset shows the optical mode distribution for different waveguide widths.

5. QD-solids for optical detection

The production of QD-solids is based on a solution-processing method called Layer-by-Layer (LbL), which is illustrated in Fig. 5.1, and preliminary results reported in Milestone 18 (MS18). These QD-solids has been successfully applied in the fabrication of infrared photodetectors and solar cells (see Refs. 2-5 as a good example). This approach allows the fabrication of smooth and crevice-free QD films directly from the colloidal solution. In a first step, we used spherical PbS QDs with for the fabrication of layer stacks and carried out their basic characterization. The key step of this method consists in a ligand exchange reaction to replace the insulating oleyamine (2 nm long) for shorter ligands. The new ligand used is bidentate in order to closely interconnect QDs. In the measure that the distance between nanocrystals is reduced, the electron and hole transport is significantly improved. It is important to note that the end functional group itself plays an important role in the passivation of the nanocrystal surface and thus the control of midgap states and shallow traps. Typically, PbS QD films were deposited on glass or glass/ITO substrates through the LbL spin-coating process. Each layer deposition consisted of four deposition steps during spinning by dropping: 1) PbS solution in octane; 2) 1% bidentate ligand solution (ethanedithiol (EDT), 3-Mercaptopropionic acid (MPA), oxalic acid, …); 3) anhydrous acetonitrile (or methanol in case of MPA); 4) anhydrous octane. We repeat these steps 4-10 times to obtain smooth quantum dot films 200-350 nm thick, as measured by using a mechanical profilometer. The optical properties are preserved after the ligand exchange, as shown in Fig. 5.2. That is, absorption and PL spectra are not very different from that measured for the colloidal solution that proves the 3D quantum size confinement of carriers after the ligand shortening. The absorption coefficient at the ground exciton state is around 3500 cm^{-1}, which means that 10 % of the incoming light at this energy range would be absorbed in a layer 350 nm thick. From XPS characterization we distinguish the sulphur-containing oxidation products polythiol S-S, lead sulphite ($PbSO_3$), and lead sulphate ($PbSO_4$), as was reported in MS18.
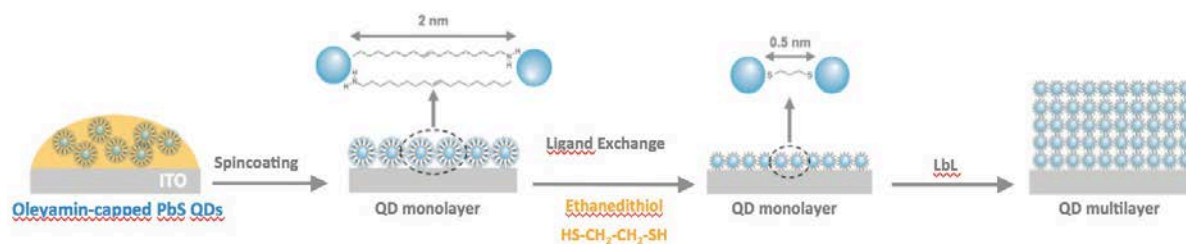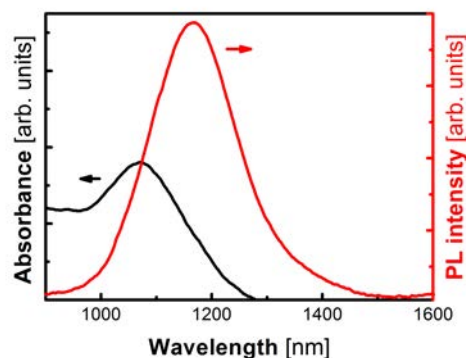

Figure 5.1: Scheme of the LBL approach.

FP7-ICT-2011-7   **Deliverable Report**
Project-No. **288869**   Last update 01/31/2012
NAVOLCHI – D4.2   Version 1

Figure 5.2: Absorption and PL spectra of EDT-capped PbS film.

Among the bidentate ligands tested for the fabrication of layer stacks, we decided to start investigating MPA instead of EDT, thioglicolic acid or oxalic acid. Ligand passivation strongly influences the charge carrier mobility, as well as recombination properties in this type of films. As reported in Ref. 32, MPA passivation may enable significant enhancement of the carrier mobility-lifetime product in the PbS QD-solid leading to an increase in both the diffusion length of charge carriers and the photon conversion efficiencies. The origin of such enhancement is due to a lower density and energetic distribution of charge traps in MPA-processed PbS QD films. Simultaneously, the lower density of charge traps decreases the bimolecular charge recombination rate in comparison to the rate expected from the increase in carrier mobility. MPA provides greater chemical diversity in comparison to EDT (presenting both thiol and carboxylate functional groups to PbS surfaces) and is therefore able to passivize a broader distribution of surface states.

Previous studies in literature developed on PbS photoconductors have shown that photosensitization of PbS is followed by oxidation, and in particular formation of lead sulphates (PbSO$_4$). They act as sensitizing centres that prolong the minority (electron) carrier lifetime allowing holes to transverse the device within this carrier lifetime. We maintain this hypothesis, but further studies will be developed to determine the generation/recombination mechanism in our material. For the moment, we have established a technological processing, as described above, for a reproducible preparation of QD solids. These layers and devices maintain their good electro-optical properties stable during weeks in air and even higher photocurrent values than the day of fabrication are obtained. This means that the QD-solid is not completely cured after 30-60 min annealing at 80-100 ºC (typical post-process treatment) and still further research is needed to understand completely the surface dynamics in this system. Preliminary characteristics of photo-electrical properties of the QD-solid in Schottky photodiodes and photoconductive devices were summarized in MS18 and more recent results will be included in Milestone 20 (MS20).

PbS and PbSe QDs can be synthesized with appropriate diameters to obtain ground exciton absorption in the near infrared (1000 – 1900 nm). QD solids based on PbS have been prepared in a reproducible way, exhibiting oxides at the QD surface and stable in air, as the photodevices fabricated with them. They exhibit appropriate photo-electrical properties for using them in photodetector devices. Best results with PbS QD-solids 360 nm thick having absorption spectra as that shown in Fig. 5.2 yield responsivities of 0.7 A/W at visible wavelengths and 1 mA/W at the ground exciton absorption wavelengths (1000-1100 nm), as reported in MS20. In the case of photoconductivity measured on similar QD-solid films deposited on glass and using lateral electrodes separated 45 µm responsivities are much lower. Further advances are expected by using smaller distances between electrodes (< 15 µm) and avoid the stability of the layers after preparation under illumination and charge transport (improving the curing process).

FP7-ICT-2011-7
Project-No. **288869**
NAVOLCHI – D4.2

Deliverable Report
Last update 01/31/2012
Version 1

6. Patternable and conducting metal-polymer nanocomposites

Conducting polymers (CPs) offer a unique combination of electric, electronic and optical properties inherent to semiconductors and metals, with the added value of processability. Polymers with a regular alternation of single and double bonds along the polymer chain (pi-conjugated polymers) form the basis of the organic CPs. With such an electronic structure, a semiconductor-like band is formed, whose band gap depends on the extension of the conjugation. The generation of charge carriers (polarons and bipolarons) can be achieved by reduction (n-doping), oxidation and protonation (p-doping) of the π-conjugated system, resulting in highly delocalized polycations or polyanions. At very low level of doping (< 1%), electrical conductivity increases several orders of magnitude up to values of around 0.1 S/cm. Subsequent doping of the CPs will result in a saturation of the conductivity in the range 1–10^4 S/cm depending on the considered polymer. Here we report new multifunctional polymeric materials, which can combine electrical conductivity and photoconductivity with other important properties, such as UV lithographic capabilities. This deliverable report deals with the demonstration of metal-(lithographic)polymer useful for: a) plasmonic nano- and micro-structures for waveguides and b) photoconductors based on Plasmonic Patternable Conductive Polymers (PPCPs). We have accomplished:

- In-situ synthesis of conducting polymer into a patternable host matrix.
- In-situ synthesis of Au nanoparticles into a patternable conducting polymer.
- Development of metallic microstructures by a chemical regrowth of metal NPs: towards prepatterned plasmonic nano- and micro-structures.

Conducting polymers with patterning capability is one of the routes (or an element) for the fabrication of a plasmonic photodetector in WP4. The first step was the synthesis of a patternable conducting polymer (PCP) based on Polyterthiophene as conducting polymer and Novolak as host matrix. This Novolak-based nanocomposite has shown good electrical properties and patterning capability by means of UV-lithography [33,34]. In a second step, a PCP containing Au nanoparticles has been also obtained using a gold salt to polymerize the terthiophene. In this case, the multifunctional material consisted of Au nanoparticles, Polyterthiophene, and PMMA as the host matrix, which can be patterned by means of E-Beam lithography. Finally, we propose an alternative method for the fabrication of metal micro/nanostructures from metal-polymer (the polymer in this case is dielectric) nanocomposite resists and their subsequent metallization by a novel wet chemistry method. A patent application on this method has been already presented [35].

Most of the information about synthesis and properties of the above given multi-functional polymers was included in Milestone 19 and hence here we will make a summary. A novel material based on Polyterthiophene as CP inside a Novolak-based negative-tone photoresist has been achieved. The nanocomposite is formed by the in-situ polymerization of terthiophene (3T) with $Cu(ClO_4)_2$ (doping agent) inside the host polymer. Conducting films in the order of 10^{-4} to 150 S/cm are obtained depending on the specific nanocomposite composition [33,34].
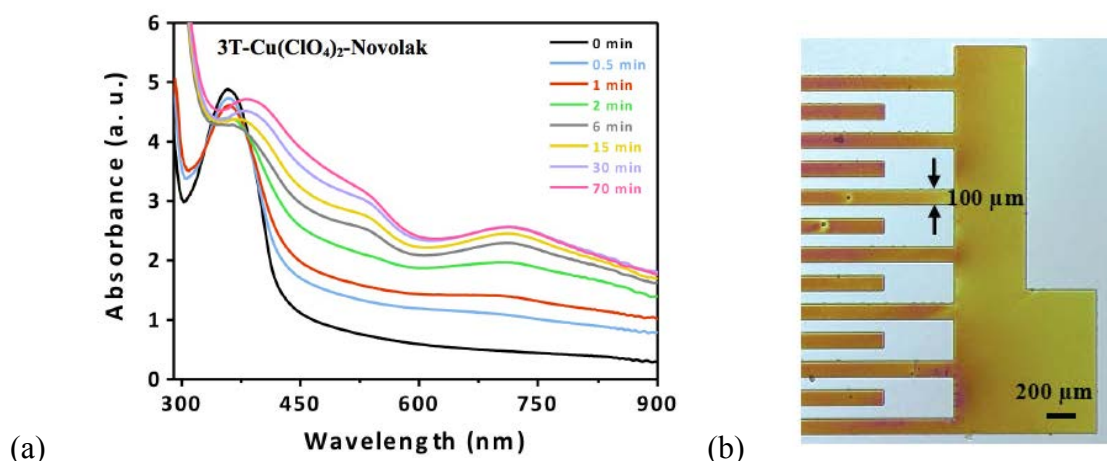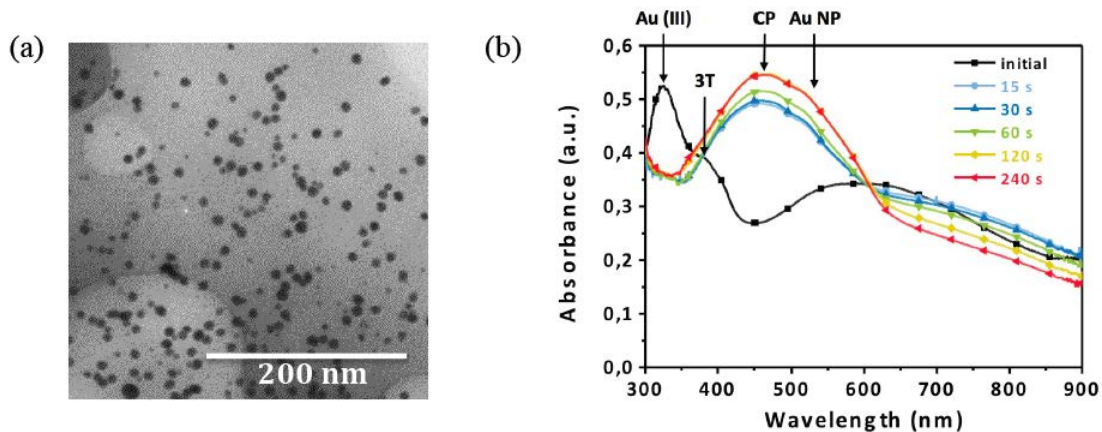
Figure 6.1: Time evolution of the absorbance spectrum for a 3T-Cu(ClO$_4$)$_2$-Novolak film after a baking process at 100 ºC (a) and example of UV-photolithography patterning (b).

The chemical oxidative polymerization of 3T exhibits a well-defined autocatalytic character, i.e. a rapid coloration and polymerization proceeds after a definite induction period. The reaction was followed by UV-Vis-NIR spectroscopy (Fig. 6.1.a). Initially, Novolak containing 3T exhibits a maximum absorption peak at around 359 nm (black line in Fig. 6.1.a). As the polymerization reaction takes place, the peak intensity of the 3T band gradually decreases and new optical absorption bands appear at the red side because of the formation of oligomers with a larger π-conjugated system. The two new bands around 535 and 715 nm gain importance during the baking process due to the formation of charge carrier bands (polaron and bipolaron) arising from the oxidation of 3T. Both polymerization and doping (oxidation) of the corresponding conjugated polymer take place simultaneously. These absorption bands would be responsible of the 3T photoconductive properties [36].

The patterning of CPs with conventional UV lithography is a significant technological challenge. Given that the polymerization of 3T into the negative-tone Novolak resist strongly affects its lithographic performance we carry out the pattern generation (UV-photolithography) and in-situ synthesis of the CP (post-bake at 100-180 ºC) in two consecutive steps of the microstructure fabrication process. The optimum formulation of the nanocomposite resist was found to be 11 wt % 3T and Cu(ClO$_4$)$_2$/3T molar ratio = 1.5. The electrical conductivity obtained with this formulation is 10^{-2} S/cm.

In a second step we have also developed a novel patternable conducting nanocomposite containing gold nanoparticles (NPs) for its possible application in plasmonic based photodetectors, where light absorbed by these nanoparticles due to their characteristic Localized Surface Plasmon Resonance (LSPR) can be transformed into an electrical current [37]. To synthesize the nanocomposite we use the same procedure as before, but this time the in-situ polymerization of 3T has been carried out using HAuCl$_4$ as oxidizing agent inside the PMMA matrix. Au nanoparticles are in-situ generated from the reduction of Au(III) to Au(0) during the bake step, as observed in Fig. 6.2.a. The in-situ synthesis of 3T and Au NPs in PMMA can be also followed by UV-Vis spectroscopy (Fig. 6.2.b). Initially, both 3T and [AuCl$_4$]$^-$ dispersed in PMMA exhibit two narrow absorption contributions at around 380 and 330 nm (black line in Fig. 4b) and a broad absorption band at 600 nm, which is attributed to the polymerization of 3T starting even at room temperature. Any absorption feature from the PMMA matrix is expected between 300 and 900 nm. However, any measurable conductivity was observed at this stage, because of the extent of the polymerization is small. As the polymerization reaction takes place, the peak intensity of the 3T red-band decreases and a new band develops at around 480 nm,

which is mixed with the LSPR absorption at 525 nm of the generated Au NPs. This new band gains importance during the baking process and the band of 3T at 600 nm broadens and shifts to longer wavelengths. This is due to the formation of charge carrier (polaron and bipolaron) bands arising from the oxidation (p-doping) of the 3T.


Figure 6.2: (a) TEM image of a nanocomposite film prepared with a molar ratio of $HAuCl_4$ to 3T equal to 1, [3T] = 0.08 M at a baking temperature of 140 ºC for 60 s; (b) Time evolution of the absorbance spectrum of a 3T−HAuCl4−PMMA film during the baking process.

Similar to the Novolak-based nanocomposite, the electrical conductivity of this metal-polymer nanocomposite also exhibits a percolating behaviour and reaches values of the order of 10 S/cm. Polymerization and doping take place simultaneously since conducting films can even be obtained with molar ratios of $HAuCl_4/3T$ as small as 0.7, which is below the stoichiometry of the reaction. Currently, the lithographic performance of this material is being optimized, but preliminary results are promising. The best result for the photoconductivity measured in these nanocomposites deposited on glass (100 nm thick) and using two electrodes separated 45 μm a give responsivities of the order of 4.10^{-4} A/W at 1 V and 0.02 A/W at 20 V (the resistivity of the film was 10 Ωcm), as shown in Fig. 6.3. In the case of the $Cu(ClO_4)_2/3T$ polymer in PMMA the photocurrent was two order of magnitude smaller, even if the resistivity in this case was two orders of magnitude higher. More investigation is being developed to have more statistics for these results.
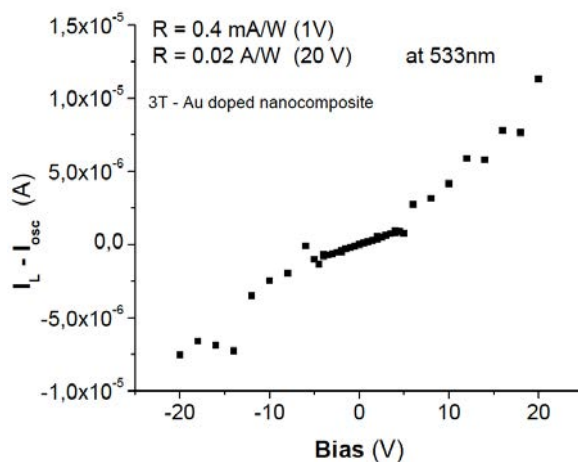
Figure 6.3: Photocurrent measured as a function of the applied bias under 533 nm illumination (0.5 mW, approximately).

FP7-ICT-2011-7   **Deliverable Report**
Project-No. **288869**   Last update 01/31/2012
NAVOLCHI – D4.2   Version 1

Finally, we have developed an alternative method for the fabrication of metal micro- and nano-structures from metal-polymer nanocomposite resists and their subsequent wet chemistry metallization. The process consists of three simple steps: (1) fabrication of macro-/micro-/nano-patterns by means of lithography or any other direct printing technologies (inkjet, microplotter, ...), (2) in-situ synthesis of metal NPs during a post-bake step and (3) wet chemistry (non-electrochemical) metallization of nanocomposite patterns. The novelty of our approach is that both metal NPs are embedded into the polymer pattern and act as seeds for the reduction of Ag(I) when immersed into a solution of the corresponding precursor metal salt ($AgNO_3$) and an appropriate reducing agent. The key point of this procedure is the use of a weak reducing agent so that the metal reduction selectively takes place at the surface of existing previously synthesized NPs. As a result, metal NPs grow significantly into the nanocomposite structure until the pattern is completely metallized.
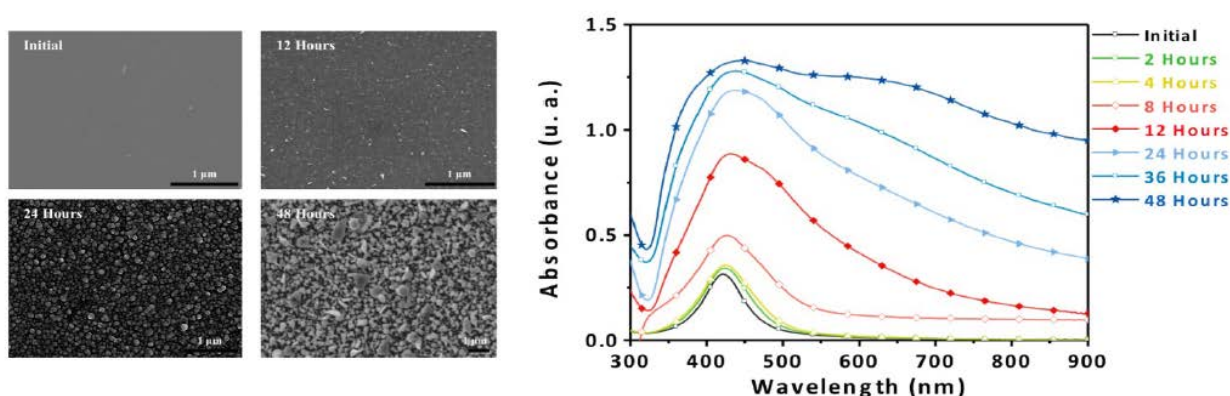
Figure 6.4: SEM images for different immersion times of the Ag-PVA nanocomposite (left) and UV-Vis spectra for different immersion times of the Ag-PVA nanocomposite in the growing solution.

The metallization process was followed by UV-Vis spectroscopy, SEM and TEM for different reaction times (Fig. 6.4). We also carried out the electrical characterization of the layers and confirmed that bulk conductivities of silver (gold in other experiments) were achieved. Given that the progress of plasmonics is closely related to the advancement of material research and fabrication technology, we believe that this fabrication method may be very useful for the fabrication of future plasmonic (waveguides for Surface Plasmon Polariton) and optolectronic (electrodes) devices.

Patterning of Ag-PVA was carried out by e-beam lithography. Figure 6.5 shows an optical microscope image of several Ag-PVA patterns (stripes 10 to 100 μm long in steps of 10 μm) generated upon exposure to an E-beam at 30 kV at doses of 2 mC/cm^2. As can be seen, the pattern absorption is significantly important after the patterning process, because of the formation of metal nanoparticles inside the PVA patterns during the e-beam irradiation. Any metallic signature is observed outside the pre-patterned Ag-PVA nano-structures (120 - 220 - 320 nm wide in left-centre-right structures of Fig 6.5). Next step will be the complete metallization of these structures by the method described above and optical characterization (excitation of surface plasmon polaritons).
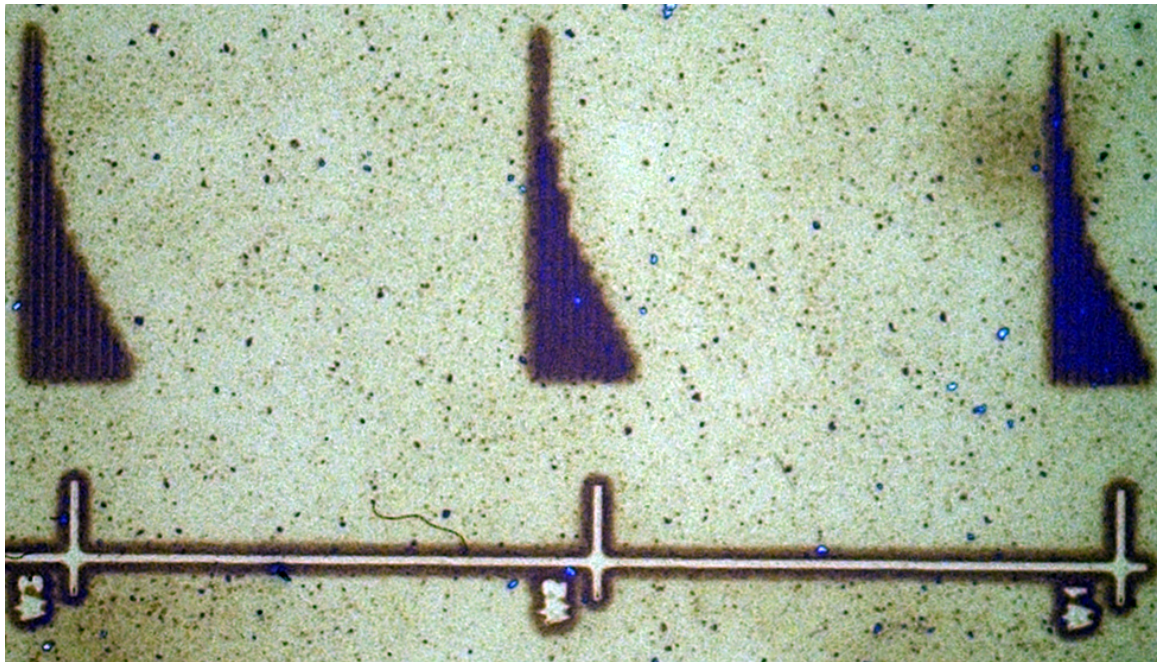
Figure 6.5: Optical microscope image of Ag-PVA nanostructures fabricated by e-beam lithography before the metallization process.

7. Conclusions and outlook

In this deliverable the optical properties of colloidal QDs and QD layers based on them have been analysed. Three approaches have been considered:

(i)   Single and few several QD-monolayer thick close packed nanocrystal films using relatively long ligands (section 3).

(ii)   Diluted QD-nanocomposite films based on QDs dispersed in dielectric polymers (section 4).

(iii)   QD-solid films by using LbL method and short ligands (section 5).

In case (i) a dipole-dipole interaction enhancement of the monolayer absorption has been demonstrated. These layers will be combined with silicon waveguides to define emitting devices by electrical injection.

In case (ii) cladding/core layers can be fabricated with QD-nanocomposites in order to define optical waveguides (1D, 2D) and get amplification on propagating surface plasmon polaritons. Gain is limited by Auger non radiative recombination and losses are determined by the QD absorption.

In case (iii) conductive layers of QDs have been achieved in order to be the base for photoconductive/photodiode devices.

Finally, a summary on patternable polymer nanocomposites (more extensively described in MS19) containing metal nanoparticles was made in section 6. A semiconducting band structure after doping with Au-ions and the formation of Au nanoparticles was observed, simultaneously. Photoconductivity have been measured in these nanocomposites and possibly enhanced by the transfer of electrons from plasmons generated at these nanoparticles. Full metallic patterned nano/microstructures can be created by using metal nanoparticle seeds that are in situ synthesized on patternable polymers.

In next months,

1)   Other QD materials will be contemplated in order to minimize Auger non radiative recombination and improve gain in QD-nanocomposites.

2)   Development of emitting devices with electrical injection compatible with silicon-based plasmonics.

3)   Metal nanostructures based on patternable polymers and use for propagating surface plasmon polaritons.

4)   Study of the photoconductivy in conducting polymers containing metal nanostructures.

FP7-ICT-2011-7
Project-No. **288869**
NAVOLCHI – D4.2

Deliverable Report
Last update 01/31/2012
Version 1

REFERENCES

[1] J. Leuthold, S. Muehlbrandt, A. Melikyan, M. Kohl, C. Koos, W. Freude, V. Dolores- Calzadilla, M. Smit, I. Suarez, J. Martínez-Pastor, E.P. Fitrakis and" I. Tomkos, "Plasmonic Communications: Light on a Wire", Optics & Photonics News, vol. May 2013, 30-35 (2013).

[2] G. Konstantatos and E.H. Sargent, "Nanostructured materials for photodetection", Nature Nanotechnology **5**, 391-400 (2010).

[3] Ferry Prins, *et al.*: "Fast and Efficient Photodetection in Nanoscale Quantum-Dot Junctions", Nano Lett. **12**, 5740–5743 (2012).

[4] F. Pelayo García de Arquer *et al.*, "Plasmonic light trapping leads to responsivity increase in colloidal quantum dot photodetectors", Appl. Phys. Lett. **100**, 043101 (2012).

[5] G. Konstantatos *et al.*, "Hybrid graphene–quantum dot phototransistors with ultrahigh gain", Nature Nanotechnology **7**, 363-368 (2012).

[6] I. Suárez, H. Gordillo, R. Abargues, S. Albert, and J. Martínez-Pastor, "Photoluminiscence wave-guiding in CdSe and CdTe QDs-PMMA nanocomposite films", Nanotechnology **22**, 435202 (2011).

[7] P. Reiss, M. Protiere, and L. Liang, "Core/Shell Semiconductor Nanocrystals", Small **5**, 154–168 (2009).

[8] E. Pedrueza, A. Segura, R. Abargues, J. Bosch, and J. P. Martínez-Pastor, "Effect of quantum size confinement on the optical properties of PbSe nanocrystals as a function of temperature and hydrostatic pressure", Nanotechnology **24**, 205701 (2013).

[9] J. E. Murphy, M. C. Beard, A. G. Norman, S. P. Ahrenkiel, J. C. Johnson, P. R. Yu, O. I. Micic, R. J. Ellingson, and A. J. Nozik, J. Am. Chem. Soc. **128**, 3241–3247 (2006).

[10] I. Moreels, K. Lambert, D. Smeets, D. D. Muynck, T. Nollet, J. C. Martins, F. Vanhaecke, A. Vantomme, C. Delerue, G. Allan, and Z Hens, ACS Nano **3**, 3023–3030 (2009).

[11] Hui Du, Chialing Chen, Rishikesh Krishnan, Todd D. Krauss, Jeffrey M. Harbold, Frank W. Wise, Malcolm G. Thomas, and John Silcox, "Optical properties of colloidal PbSe nanocrystals", Nanoletters **2**, 1321-1324 (2002).

[12] Moreels, I. *et al.* Size-Tunable, Bright, and Stable PbS Quantum Dots: A Surface Chemistry Study. *Acs Nano* **5**, 2004-2012 (2011).

[13] Justo Y *et al.* Multiple Dot-in-Rod PbS/CdS Heterostructures with High Photoluminescence Quantum Yield in the Near-Infrared. *Journal of the American Chemical Society* **134**, 5484-5487 (2012).

[14] Schaller, R. D., Petruska, M. A. & Klimov, V. I. Tunable near-infrared optical gain and amplified spontaneous emission using PbSe nanocrystals. *Journal of Physical Chemistry B* **107**, 13765-13768 (2003).

[15] Htoon, H., Hollingworth, J. A., Malko, A. V., Dickerson, R. & Klimov, V. I. Light amplification in semiconductor nanocrystals: Quantum rods versus quantum dots. *Applied Physics Letters* **82**, 4776-4778 (2003).

[16] V. I. Klimov *et al.*, "Single-exciton optical gain in semiconductor nanocrystals". *Nature* **447**, 441-446 (2007).

[17] B. De Geyter *et al.*, "The Different Nature of Band Edge Absorption and Emission in Colloidal PbSe/CdSe Core/Shell Quantum Dots", *ACS Nano* **5**, 58-66 (2011).

[18] A. M. Dennis *et al.*, "Suppressed Blinking and Auger Recombination in Near-Infrared Type-II InP/CdS Nanocrystal Quantum Dots", Nano Lett. **12**, 5545–5551 (2012).

[19] Capek, R. K. *et al.* Optical Properties of Zincblende Cadmium Selenide Quantum Dots. *The Journal of Physical Chemistry C* **114**, 6371–6376 (2010).

[20] Justo, Y., Moreels, I., Lambert, K. & Hens, Z. Langmuir-Blodgett monolayers of colloidal lead chalcogenide quantum dots: morphology and photoluminescence. *Nanotechnology* **21**, 295606 (2010).

[21] Pietryga, J. M. *et al.* Utilizing the Lability of Lead Selenide to Produce Heterostructured Nanocrystals with Bright, Stable Infrared Emission. *Journal of the American Chemical Society* **130**, 4879-4885 (2008).

[22] Moreels, I. *et al.* Dielectric function of colloidal lead chalcogenide quantum dots obtained by a Kramers-Kronig analysis of the absorbance spectrum. *Physical Review B* **81**, 235319 (2010).

[23] J. M. Ruano-López, M. Aguirregabiria, M. Tijero et al., "A new SU-8 process to integrate buried waveguides and sealed microchannels for a Lab-on-a-Chip", Sensors and Actuators B **114**, 542–551 (2006).

[24] http://www.microchem.com/Prod-SU8 KMPR.htm.

[25] C. B. Murray, C. R. Kagan, and M. G. Bawendi, "Synthesis and characterization of monodisperse nanocrystals and closepacked nanocrystal assemblies", Annual Review of Materials Science **30**, 545–610 (2000).

[26] V. M. Menon, S. Husaini, N. Valappil, and M. Luberto, "Photonic emitters and circuits based on colloidal quantum dot composites", 6th Conf. on Quantum Dots, Particles, and Nanoclusters, Proceedings of SPIE, vol. 72224, 1–8 (2009).

FP7-ICT-2011-7
Project-No. **288869**
NAVOLCHI – D4.2

Deliverable Report
Last update 01/31/2012
Version 1

[27] H. Gordillo, I. Suárez, R. Abargues, P. Rodríguez-Cantó, S. Albert and J.P. Martínez-Pastor, "Polymer/QDs nanocomposites for wave-guiding applications", Journal of Nanomaterials, **Vol. 2012**, Article ID 960201 (doi:10.1155/2012/960201), 1-9 (2012).

[28] H. Gordillo, I. Suárez, R. Abargues, P. Rodríguez-Cantó and J.P. Martínez-Pastor, "Color tuning and white light by dispersing CdSe, CdTe and CdS in PMMA nanocomposite waveguides", IEEE Photon. J. **5**, 2201412 (12 pgs) (2013).

[29] I. Suárez, H. Gordillo, R. Abargues, P. Rodríguez-Cantó, G. Almuneau and J.P. Martínez-Pastor, "Quantum-dot double layer polymer waveguides by evanescent light coupling", IEEE/OSA Journal of Lightwave Technology, under revision.

[30] L. Dal Negro, P. Bettotti, M. Cazzanelli, D. Pacifi and L. Pavesi, "Applicability conditions and experimental analysis of the variable stripe length method for gain measurements", Optics Communications **229**, 337-348 (2004).

[31] J. J. Jasieniak, I. Fortunati, S. Gardin, R. Signorini, R. Bozio, A. Martucci and P. Mulvaney, "Highly efficient amplified stimulated emission from CdSe-CdS-ZnS quantum dot doped waveguides with two-photon infrared optical pumping", Advanced Materials **20**, 69-73 (2008).

[32] K. S. Jeong, J. Tang, H. Liu, *et al.,* "Enhanced mobility-lifetime products in pbs colloidal quantum dot photovoltaics", ACS Nano **6**, 89-99 (2012).

[33] R. Abargues, P. J. Rodríguez-Cantó, R. García-Calzada, and J. Martínez-Pastor, "Patterning of conducting polymers using UV lithography: the in-situ polymerization approach" J. Phys. Chem. C, vol. 116, pp. 17547-17553, 2012.

[34] P. J. Rodríguez-Cantó, R. Abargues, R. García-Calzada, and J. Martínez-Pastor, "UV-Patterning of In Situ Synthesized Conducting Polymers for Polymeric Display Devices", submitted to *Synthetic Metals J.*

[35] R. Abargues, P. Cantó Rodríguez, M. L. Martínez Marco, J. Martínez Pastor, and J. L. Valdés, "Method to obtain metallic structures of nano- and micro-metric size from lithographic resists based on nanocomposites", Application No. P201201282, Spain, 28/12/2012, Owners: University of Valencia (50 %), Intenanomat SL (50 %).

[36] G. Horowitz, F. Kouki, P. Valat, P. Delannoy, and J. Roussel, "Photoconductivity of sexithiophene single crystals", Phys. Rev. B **59**, 10651-10656 (1999).

[37] S. Mubeen, G. Hernandez-Sosa, D. Moses, J. Lee, and M. Moskovits, "Plasmonic Photosensitization of a Wide Band Gap Semiconductor: Converting Plasmons to Charge Carriers," Nano Lett. **11**, 5548–5552 (2011).